Potassium citrate-activated pure BOF slag-based mortars utilizing carbonated and autoclaved BOF slag aggregates

Cement and Concrete Composites 150 (2024) 105564

Contents lists available at ScienceDirect

Cement and Concrete Composites

journal homepage: www.elsevier.com/locate/cemconcomp

Potassium citrate-activated pure BOF slag-based mortars utilizing carbonated and autoclaved BOF slag aggregates

Zhihan Jiang [a], Jonathan Zepper [a,b], Xuan Ling [a,*], Katrin Schollbach [a], H.J.H. Brouwers [a]

[a] Department of the Built Environment, Eindhoven University of Technology, Eindhoven, 5600, MB, the Netherlands
[b] Tata Steel, TEC, Centre of Expertise Steelmaking and Casting, PO Box 10.000, 1970, CA, IJmuiden, the Netherlands

ARTICLE INFO

Keywords:
BOF slag
Tri-potassium citrate
Carbonation
Autoclaving
Interfacial transition zone (ITZ)
Leaching

ABSTRACT

This study proposes novel basic oxygen furnace (BOF) slag mortars formulated with tri-potassium citrate (TPC) activated BOF slag as binder and treated BOF slag (carbonated (CB) and autoclaved (AB)) as aggregates, aiming to maximize the utilization of BOF slag in the construction industry. Untreated BOF slag (UB) and natural sand (NS) were employed as reference aggregates. The effects of carbonation and autoclaving were investigated, focusing on the interfacial transition zone (ITZ) properties through SEM-BSE greyscale thresholding and constituent segmentation analysis. Results indicate that both treatments reduce the free CaO, promote $CaCO_3$ formation, and modify the aggregate surface. The 28 d compressive strength of pure BOF slag-based mortars with UB, CB, and AB aggregates are 25.8, 29.4, and 34.8 MPa (average at varying TPC dosages), significantly higher than that with NS (19.6 MPa). Pure BOF slag-based mortars also show narrower ITZ thicknesses and the absence of bond cracks. Mortars with CB and AB aggregates exhibit fewer unreacted particles and more hydration products within the integral binder region compared to those with UB. Overall, pure BOF slag-based mortars present a more robust aggregate/binder interface that is further enhanced by the aggregate treatments. Leaching values of all mortars are well below the Dutch legal limits. The findings suggest promising application prospects for pure BOF slag-based mortars in substituting cement mortars and valorizing BOF slag.

1. Introduction

Basic oxygen furnace (BOF) slag, also known as converter steel slag, is the waste material generated during the Linz-Donawitz steel-making process in the basic oxygen furnace [1]. It is mainly composed of CaO (30–50 %), SiO_2 (10–20 %), Fe_2O_3 (20–40 %), Al_2O_3 (1–7%), MgO (4–10 %), MnO (0–4%), P_2O_5 (1–3%) and TiO_2 (0–2%) [1–3]. The main mineral phases typically include belite (C_2S) and a small amount of alite (C_3S) (for some BOF slag), brownmillerite ($C_2(A,F)$), magnetite, RO phase (FeO-MgO-MnO solid solution, in wuestite structure), and free lime (CaO) [2,4,5]. The world crude steel production in 2022 is nearly 1.9 billion tons, and 71.5 % comes from the basic oxygen furnace steelmaking process [6]. Although calcium silicates (mainly C_2S) and $C_2(A,F)$ in BOF slag provide potential cementitious ability, their hydration reactivity is relatively low, which impedes BOF slag utilization as a binder material [2,7]. For utilization as aggregate, due to the presence of free lime (f-CaO), volume instability can be a fatal problem [8–12]. The delayed hydration of f-CaO after cement hardening may cause mortar or concrete cracks or directly destroy the material [1,13]. It needs to be noted that even though free MgO could be a potential hazard for volume soundness, due to the high basicity in molten BOF slag and the close radii of Mg^{2+}, Fe^{2+}, and Mn^{2+} (0.78, 0.83, and 0.91 Å), MgO primarily forms an RO solid solution with FeO and MnO in wuestite structure, free MgO (periclase) rarely forms [14], especially not in the BOF slag that we used in this investigation from Tata Steel, as characterized in detail before [15–17]. The presence of heavy metals (mainly vanadium and chromium) and their potential leaching also hinder the use of BOF slag [1,18]. Most are landfilled or utilized in low-end applications, leading to massive yearly accumulation. It may cause severe problems such as land waste and pollution of soil and water.

Investigations have been conducted to improve or activate the hydration reactivity of BOF slag. Hu et al. found a BOF slag-Metakaolin binder system (80 % MK and 20 % BOF slag) activated by sodium silicate solution presented higher early and late age strength than MK and plain cement samples [19]. Wang and Yan accelerated the early-age hydration of BOF slag by increasing the fineness of particles and curing temperatures, as well as the alkalinity (by adding NaOH).

* Corresponding author.
E-mail address: x.ling@tue.nl (X. Ling).

https://doi.org/10.1016/j.cemconcomp.2024.105564
Received 1 March 2024; Received in revised form 24 April 2024; Accepted 27 April 2024
Available online 29 April 2024

However, increasing the pH value of the solution had little effect on the later hydration of the slag, and raising the curing temperature even negatively influenced its later hydration [20]. Belhadj et al. indicated that $CaCl_2$ can accelerate the hydration of BOF slag with doubled compressive strength compared to the pure BOF slag sample [21]. However, these results are not convincing enough to utilize BOF slag as a cementitious material at a large scale [19–26]. Kaja et al. made a high-strength BOF slag binder (75 MPa of compressive strength after 28 days of hydration) with tri-potassium citrate (TPC) as the activator, indicating the great potential of utilizing BOF slag as a sustainable binder [2]. Likewise, some methods have been proposed to eliminate or mitigate the (potential) volume unsoundness when BOF slag is used as aggregate, such as natural aging, carbonation, and autoclaving [11,13,27,28]. Natural aging is easy to accomplish and does not require special equipment and processes. However, it is time-consuming, and the extended stacking of BOF slag may cause the leaching of heavy metals into the environment [13]. Carbonation and autoclaving show satisfying effects on ensuring the volume soundness of mortar or concrete incorporating BOF slag aggregates [11,27–29]. Besides, these two treatments are easy to process and consume little time.

In this research, novel cement-free mortars composed entirely of BOF slag serving as both binder and aggregate were proposed and investigated to achieve the maximum consumption of BOF slag and efficient use in the construction industry. The high specific density and hardness of such a building material can make it suitable for numerous particular constructions, such as road pavement, railway track beds, and coastal protection [22,30–32]. The mortar is based on the TPC-activated BOF slag binder [2] and carbonated and autoclaved BOF slag aggregate (CB and AB). For this purpose, the unreacted BOF slag was initially pre-treated with carbonation and autoclaving processes, respectively. Natural sand (NS) and untreated BOF slag (UB) were utilized as the reference. Carbonation and autoclaving effects on the BOF slag aggregate were characterized, and the impacts on the integral properties of pure BOF slag-based mortars, such as compressive strength and leaching properties, were studied. Most importantly, in this paper, the interfacial transition zone (ITZ) properties of the TPC-activated BOF slag binder system were investigated for the first time, especially within pure BOF slag-based systems where aggregates were also BOF slag. This is vital since the ITZ between aggregate and binder matrix is typically considered a critical weak region where cracks initiate and propagate for cementitious composites like mortar or concrete [33–42]. Multiple techniques were used, such as XRD and quantitative Rietveld refinement, thermalgravimetric (TG/DTG) analysis, titration based on the ethylene glycol method, nitrogen (N_2) adsorption/desorption tests (NAT), and scanning electron microscopy (SEM). The leaching of heavy metals was measured through a one-stage leaching operation combined with inductively coupled plasma atomic emission spectroscopy (ICP-AES). The ITZ research was conducted mainly based on SEM-backscattered electron (BSE) image analysis (with the application of an in-house MATLAB code) and energy dispersive x-ray spectrometer (EDS) analysis. The aggregate/binder edge was identified first in BSE images shot around the aggregate/binder boundary. Then, successive strips along this edge (within the area of the binder) were delimitated. Finally, constituents (pores, hydration products, unreacted particles) of these strips were quantified based on grayscale thresholding. In summary, this research proposed and investigated a pure BOF slag-based mortar system based on TPC-activated BOF slag binder and carbonated or autoclaved BOF slag aggregates for the first time. The effects of BOF slag aggregate carbonation and autoclaving on various significant properties, especially the ITZ properties, were studied. The study shows that the large-scale application and valorization of BOF slag (typically regarded as a solid waste) as building materials may be possible and reduce the reliance on traditional high-carbon-emitting building materials such as cement and crushed rock aggregate.

2. Materials and methods

2.1. Raw materials and activator

The BOF slag used in this research was collected from the standard steel production of Tata Steel (Netherlands). For binder application, it was milled by a vibratory disc mill (RS 300 XL, Retsch) at 1 kg/15 min. Fig. 1 shows the particle size distribution of BOF slag powder after milling (D_{50} = 18 μm), measured by laser diffraction spectroscopy (Mastersizer 2000, Malvern). It is similar to the typical particle size distribution of traditional Portland cement, varying from less than 1 μm–100 μm [43,44].

The quantitative chemical and mineralogical compositions of BOF slag were characterized by XRF (Axios, PANalytical) and XRD analysis (D8 Endeavor, Bruker) with the Co Kα as the radiation source to avoid fluorescence and Si as internal standard and quantified by Rietveld refinement (TOPAS, Bruker), as presented in Table 1. C_2S, wuestite, brownmillerite, and magnetite are the main minerals. Tri-potassium citrate monohydrate ($K_3C_6H_5O_7{\cdot}H_2O$, GPR RECTAPUR®, purity >99 %) used as the activator was purchased from VWR Chemicals.

The natural sand (NS) used in the experiment was sieved from pre-bagged CEN standard sand (1350 g per bag), conforming to EN 196-1 [45]. It is worth mentioning that aggregate size or size distribution obviously affects ITZ properties [35,39,46–48]. Thus, to eliminate the influence aggregate size on the final ITZ properties, NS and UB were sieved and the grains with particle size (1–2 mm) were utilized as aggregates. The difference between aggregates and binder is significant sufficient to identify ITZ clearly.

2.2. Carbonation and autoclaving of BOF slag aggregate

Carbonation and autoclaving were conducted separately on parts of sieved-out 1–2 mm UB grains. Based on preliminary tests and existing studies, the carbonation process was conducted in a CO_2 climate chamber (ICH260C, Memmert) with 20 % CO_2 concentration, 80 % relative humidity, and 50 °C for 3 days [49–52]. Also, according to existing research and pre-tests, the autoclaving was conducted in a 400 Liter Scholz saturated steam autoclave for 8 h, with the temperature and pressure peaking at 187 °C and 11 bar [12,27,53]. Four types of aggregates (NS, UB, CB, and AB) were placed into the vacuum oven at 40 °C for two days before usage for drying. The relatively low drying temperature was chosen to avoid damaging any potential reaction products after treatments.

To characterize the effects of BOF slag aggregate carbonation and

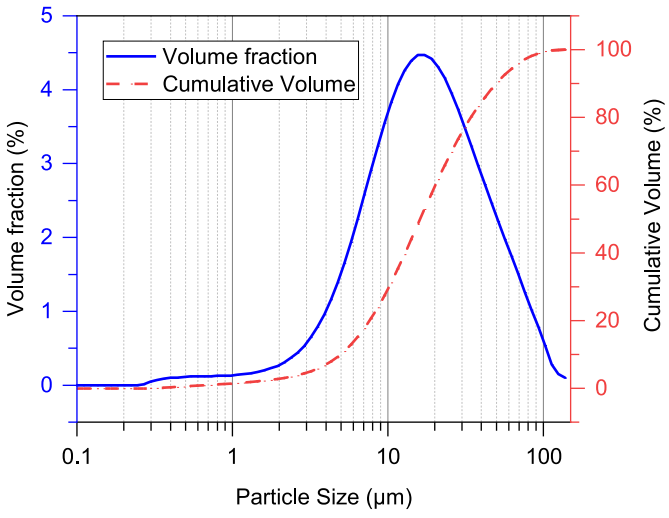

Fig. 1. Particle size distribution of milled BOF slag.

Table 1
Mineralogical and chemical composition of BOF slag.

Mineral compositions	Content (wt %)	Chemical compositions	Content (wt %)
C_2S (α' + β)	38.3	CaO	40.54
Wuestite	21.9	Fe_2O_3	26.52
Brownmillerite	18.0	SiO_2	14.50
Magnetite	8.6	MgO	7.56
C_3S	1.7	MnO	4.52
Calcite	1.0	Al_2O_3	1.77
Dolomite	0.9	TiO_2	1.64
Free Lime	0.7	V_2O_5	0.93
Portlandite	0.5	P_2O_5	1.61
Others[a]	0.8	Cr_2O_3	0.30
Amorphous	7.6	Na_2O	0.11
		GOI[b] 1000	1.4

[a] Some minor phases like Fe-perovskite and metallic iron are categorized as "others".
[b] mass gain of ignition (GOI) after BOF slag is heated up to 1000 °C in air, which could be due to the oxidation of metallic oxides, such as divalent iron.

autoclaving treatments, the dried UB, CB, and AB 1–2 mm grains were observed using a vacuum SEM (Phenom ProX, Thermo Fisher Scientific). Part of the dried grains was put into the "SmartPrep" degassing system (TriStar II 3020, Micromeritics) and degassed by Helium for 4 h. Then the N_2 adsorption/desorption tests of the three types of BOF slag aggregates were conducted based on the surface area and pore distribution analyzer (TriStar II 3020, Micromeritics) at 77.3 K. Some dried grains were milled into powder by a planetary ball mill (Pulverisette 5, Fritsch) and then analyzed by the XRD (D8 Endeavor X-ray Diffractometer, Bruker) and TG (STA 449 F1 Jupiter, NETZSCH). Part of the powder was sieved below 100 μm and then placed in the ethylene glycol (60 °C bath for 30 min) and titrated by the N/10 HCl standard solution (with the brome-cresol green solution as the indicator) to quantify the free CaO precisely [54,55].

2.3. Specimens

2.3.1. Mix design

Four series of mortars were formulated with four types of aggregate at three TPC dosages, respectively. Based on the preliminary test results, all water/binder (BOF slag powder) mass ratios were set at 0.18 to achieve suitable workability and mechanical strength. Meanwhile, to minimize the overlapping of ITZ caused by the adjacent aggregate [48,56], thus showing a clear and distinct ITZ, the volume fractions of aggregate and binder within all mortars were set constant to 20 % and 80 %, respectively. The detailed mix design is shown in Table 2. All mortars were tested and characterized after 28 days of hydration.

2.3.2. Specimen preparation

First, TPC was mixed with deionized water for each specimen. After that, the TPC solution was added to BOF slag powder, and the paste was mixed for 2 min at high speed in a mixer conforming to EN196-1 [57]. Then, the aggregates were added to the paste for another 2 min high-speed mixing. The fresh mortar was then cast into 40 mm × 40 mm × 160 mm prism molds and vibrated 30 times in the jolting apparatus, conforming to EN196-1 [57]. Thereafter, it was covered with plastic films to prevent evaporation and placed in the curing room (20 °C ± 1 °C and 95 % RH) for 1 day before demoulding [57]. Finally, the specimens were demoulded, sealed with plastic films, and cured until testing age. Each specimen had 4 replicates: 3 for compressive strength and subsequent leaching tests and 1 for ITZ analysis. At the end of the curing period, replicates for compressive strength tests were tested directly after the removal of films, according to EN 196-1 [57]. Residual fragments were crushed and sieved below 4 mm for the leaching test. Deionized water was mixed with the sieved fragments at a liquid-to-solid ratio of 10 l/kg following EN12457-1 [58]. The mixture was shaken in the shaker (ES SM-30, Edmund Buhler) for 24 h and centrifuged to separate the solid and leachate. The leachate was filtered by syringe filters and acidified, and finally, analyzed by an inductively coupled plasma atomic emission spectrometer (ICP-AES, SPECTROBLUE).

Table 2
Mix design of BOF slag-based mortars.

Specimen	Aggregate (20 vol% of mortar)	Activator content (wt% to binder)
NS1	Natural Sand	1
NS3		3
NS5		5
UB1	Untreated BOF slag	1
UB3		3
UB5		5
CB1	Carbonated BOF slag	1
CB3		3
CB5		5
AB1	Autoclaved BOF slag	1
AB3		3
AB5		5

The replicate for ITZ analysis was cut perpendicular to the casting direction in the central part by a diamond saw with a water-lubrication system. The cut portion was further cut into smaller cube pieces with a side length of around 10 mm, as shown in Fig. 2, to fit into 1-inch diameter rubber molds for SEM analysis. The cut cube piece was immersed in isopropanol for 2 days to stop hydration and then put in the vacuum drying oven at 40 °C for 24 h. Then, it was impregnated with low-viscosity epoxy resin (EpoxiCure™ 2, BUEHLER) and cured in a drying oven at 40 °C for 2 days. The hardening epoxy-impregnated sample was polished using the polish machine (Tegramin-30, Struers) in a specialized program with progressively finer polish disks (down to 1 μm) and corresponding diamond suspensions [39,40,42,59].

The well-polished epoxy sample was sputter-coated (Q15OTS, Quorum Technologies) with a gold layer on the top surface and painted with silver conductive paint on the side face to improve conductivity. The vacuum SEM (Phenom ProX, Thermo Fisher Scientific), equipped with BSE and SE detectors and an EDS spectrometer, was utilized. The BSE images were greyscale images where pixels have 256 greyscale levels (from 0 black to 255 white) obtained at an acceleration voltage of 15 kV and 1000 × magnification. Thirty frames of BSE images were taken randomly around different aggregate edges for each mortar. Each image consisted of 2048 × 2176 pixels that were 0.13 by 0.13 μm each. Thus, the pores below 0.13 μm could not be identified. Moreover, at most, two images were taken around one aggregate edge to guarantee unbiased sampling and statistical reliability [59]. The EDS map analysis was conducted around the representative aggregate boundary. EDS spot analysis was executed after ITZ thickness was determined for each sample [42].

2.4. Image process

Image processing and analysis were conducted to determine and analyze the properties of ITZ within each mortar. The steps mainly include edge identification, strip delimitation, and constituent quantification.

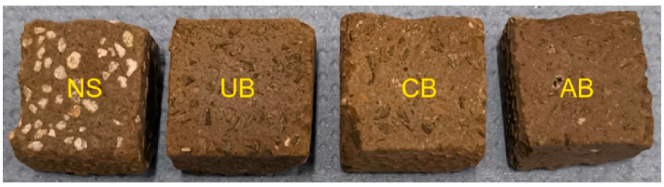

Fig. 2. Cubic mortar pieces for SEM analysis.

2.4.1. Edge identification

There are limited studies about aggregate segmentation or edge identification, such as greyscale thresholding combined with morphology operations to machine learning methods like K-means clustering or convolutional neural networks [60–62]. It is still challenging to identify the aggregate edge automatically due to the typically close grey level of binder and aggregate in BSE images combined with the irregular outline of aggregate [59,63]. The situation is even more difficult for this research, where both the binder and aggregate are BOF slag. Thus, an artificial method was applied to define the edge of the aggregate. The aggregate boundary was identified and labeled with a multi-point line, as shown in Fig. 3a. After that, the aggregate was removed from the BSE image. The aggregate-removed binder is as shown in Fig. 3b.

2.4.2. Strips delimitation

After determining the aggregate edge, successive strips were delimited along the aggregate boundary based on the "concentric expansion" method to quantitatively characterize the ITZ properties at specific distances from the aggregate edge [59]. Twelve successive 5 μm strips were delimited within one BSE image in total, as presented in Fig. 3c, and the operations were repeated for all 30 BSE pictures of each mortar specimen. Then, successive strips were clipped from the BSE image separately, as seen in Fig. 3d, and put in the folder where the aggregate-removed binder BSE image is located for further quantification analysis.

2.4.3. Constituent quantification

The phases with higher average atomic numbers within BSE images have higher grey values (i.e., lighter in the image) [34,64–66]. Thus, the binder could be segmented into three constituents: pores, hydration products, and unreacted particles in order of grayscale from small to large (aggregate removed). Due to the size restriction of a single pixel, the ''pores'' here refer to voids above 0.13 μm filled by epoxy resin, including capillary pores and micro-cracks [42,67]. Wong et al. proposed the classic ''overflow'' criteria to determine the upper threshold grayscale of pores [67]. Edwin et al. improved it [68]. However, the ''overflow'' criteria (or improved version) requires a separate calculation of the inflection point and can only segment the pores. Hence, in this research, the grayscale thresholding and segmentation were based on the ''OTSU" (named after Nobuyuki Otsu) algorithm [69], maximizing the between-class variance to threshold grayscale levels. The updated and extended ''OTSU'' algorithm was applied for faster computation and multilevel thresholding: pores, hydration products, and unreacted particles [70].

3. Results and discussion

3.1. Effects of carbonation and autoclaving on BOF slag aggregate

Table 3 gives the quantitative XRD analysis results of untreated, carbonated, and autoclaved BOF slag aggregates (UB, CB, and AB) by XRD spectra analysis and Rietveld refinement. The main components of the three types of BOF slag aggregate are the same: C_2S, brownmillerite, wuestite, and magnetite. Both treatments promote the formation of $CaCO_3$, especially carbonation. $CaCO_3$ within CB and AB increases by 264 % and 200 % compared to UB, respectively. The amorphous appears to be the principal reacting phase during the two treatments, with a 47 % and 49 % reduction for CB and AB compared to UB, respectively. Notably, due to the slow cooling rate and chemical composition, BOF slag is typically highly crystalline after solidification [16,71]. The presence of the amorphous phase is primarily attributed to the milling process applied to the raw materials. As indicated by the large-area phase mapping analysis based on PhAse Recognition and Characterization (PARC) software and XRD Rietveld refinement in Ref. [2], the main decreasing phase after milling is C_2S. It could be inferred that some crystalline C_2S becomes amorphous during milling here. It is likely more reactive during carbonation and autoclaving treatments. Therefore, the increase in calcium carbonates should be primarily due to the carbonation of amorphous C_2S. The reduction in free lime content seems to be limited. Considering the limitations of Rietveld refinement in accurately determining the minor phase, the ethylene glycol method was conducted [54,55], and the values are presented in Table 3. It is clear that after both carbonation and autoclaving treatments, the free lime was reduced significantly. The content of portlandite also decreases slightly due to the treatments.

TG and DTG experiments were also conducted from 40 °C to 1000 °C at the heating rate of 20 °C/min, as shown in Fig. 4. The weight of UB, CB, and AB aggregate decreases only 1.2 wt%, 1.7 wt%, and 1.5 wt%,

Table 3
Mineralogical composition of BOF slag aggregates.

Phases	UB	CB	AB
Wuestite	21.6	22.1	22.3
Magnetite	8.9	9.4	9.4
Brownmillerite	18.6	18.9	18.9
C_2S (α' + β)	37.2	37.0	37.4
C_3S	3.2	3.0	3.5
Free Lime	0.9 [0.7]	1.0 [0.2]	0.9 [0.1]
Portlandite	0.6 (0.8)	0.4 (0.5)	0.3 (0.6)
$CaCO_3$	1.1 (0.8)	4.0 (2.5)	3.3 (1.6)
Amorphous	7.9	4.2	4.0

[] The content of free CaO calculated by the total CaO (calculated by the ethylene glycol method) subtracted the portlandite content (from TG/DTG analysis); () amount of portlandite and calcium carbonates determined by TGA (tangential method).

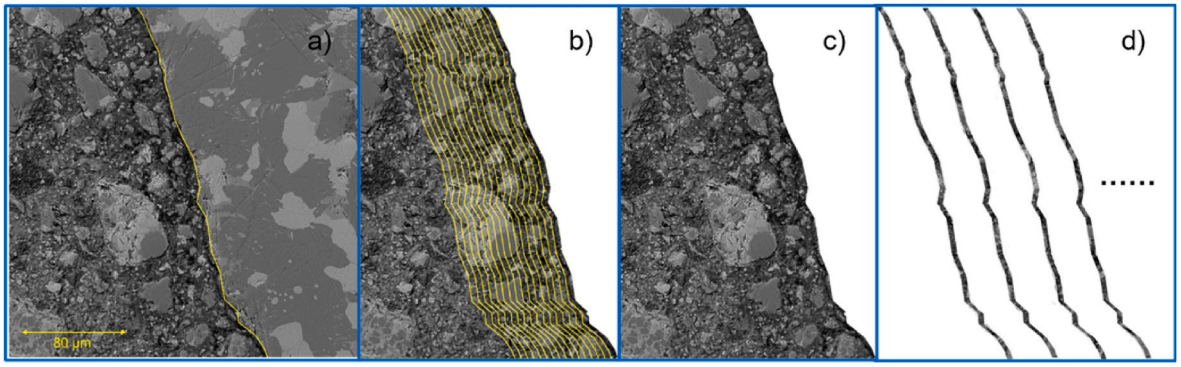

Fig. 3. The schematic diagram for the processing of a typical BSE image.

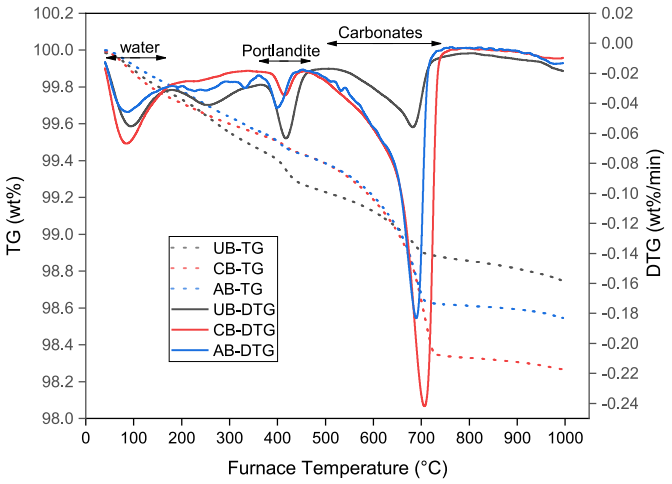

Fig. 4. TG/DTG analysis of three types of BOF slag aggregate.

respectively, after the whole process. Treatments slightly increase overall weight loss. The weight loss between 400 °C and 415 °C can be attributed to portlandite dehydration, and treated aggregates show slight portlandite depletion after carbonation and autoclaving. The portlandite content could be determined as 0.8 wt%, 0.5 wt%, and 0.6 wt% for UB, CB, and AB, respectively, according to the weight loss. The weight loss ranging from 680 °C to 710° is attributed to the carbonate decomposition, indicating that both carbonation and autoclaving treatments increase carbonate formation. The carbonate content is 2.5 wt% and 1.6 wt% within CB and AB, respectively, compared with only 0.8 wt% for UB. Mass loss observed during temperatures ranging from 40 °C to around 150 °C is relatively low (about 0.2 wt%) and can be assigned to the residual physically or chemically bound water. TG and DTG analysis confirm the increase of carbonates and the minor drop of portlandite due to carbonation and autoclaving, exhibiting the same trend as the QXRD results.

Fig. 5 presents the N_2 adsorption/desorption isotherms of the three kinds of BOF slag aggregates: UB, CB, and AB. According to the IUPAC classification, all isotherms are the ''II'' type of isotherm and have the H3 hysteresis [72]. Thus, the Brunauer-Emmett-Teller (BET) method and Barrett-Joyner-Halenda (BJH) method (based on the adsorption branch) were utilized to characterize the specific surface area (S_{BET}) and pore properties, respectively [73,74]. When the size of pores increases from 100 nm to above, the accuracy cannot be guaranteed, as a tiny difference in relative pressure is needed in this situation to differentiate the pore size [75,76]. For example, P/P_0 increases by 0.005 as pore size rises from 100 to 200 nm [75]. Therefore, 1.7–120 nm data were utilized in the research, according to Ref. [77]. Table 4 shows the S_{BET} and pore characteristics of three types of BOF slag aggregates. The S_{BET} of CB and AB is lower compared with that of UB but very similar to each other. The cumulative pore volume of CB and AB is lower by 52 % and 32 %, compared to UB, respectively. The average pore width of CB is also 37 % smaller than that of UB. In contrast, the average pore width of AB is just slightly lower than that of UB.

Fig. 6 presents the differential pore width distribution curves (up to 120 nm) of the three BOF slag aggregates. As shown in Fig. 6, CB and AB have much lower pore distribution for any pore width range above 10 nm than UB, and CB presents obviously lower values than AB. Based on the above N_2 adsorption/desorption analysis, it can be inferred that the pores of BOF slag aggregate are filled and refined after carbonation and autoclaving, which leads to the drop of S_{BET} simultaneously. Combining the QXRD and TG analysis, the main filling phase of pores is most likely to be calcium carbonate.

Fig. 7 shows the typical SEM-SE images (at 10000 × magnification) of the surface of three BOF slag aggregates (UB, CB, and AB), exhibiting the evident surface morphology alteration caused by carbonation and autoclaving. After carbonation or autoclaving, both CB and AB present an uneven products-enriched out-layer in Fig. 7b and c. Table 5 presents the chemical compositions of reaction products on the surface of CB and AB aggregates (labeled in Fig. 7) acquired by EDS spot analysis. It can be inferred from Table 5 that calcium carbonates are the main reaction products, either after carbonation or autoclaving, which is consistent with the QXRD and TG/DTG analysis. Based on the morphology of the treatment products in Fig. 7, the polymorphs of calcium carbonates within CB and AB could be mainly needle-like or columnar aragonite (with a little bit of spherical vaterite), and rhombohedral or scalenohedral calcite, respectively, as similar morphologies reported in Refs. [78–80].

Overall, carbonation and autoclaving of BOF slag aggregate reduce the free CaO, promote the formation of calcium carbonates, and decrease the amorphous phase that is most likely formed by unstable C_2S during milling. Meanwhile, aggregate pores are filled and refined most likely by calcium carbonate formation with an apparent decline of

Table 4
Surface and pore characteristics obtained from N_2 adsorption tests.

Aggregate	S_{BET} (m^2/g)	Cumulative pore volume (cm^3/g)	Average pore width (nm)
UB	0.59	0.0031	24.2
CB	0.41	0.0015	15.3
AB	0.40	0.0021	22.5

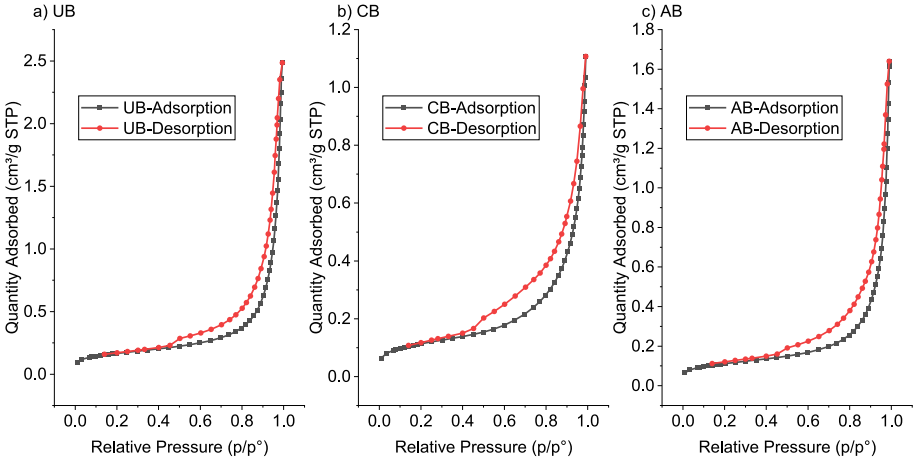

Fig. 5. N_2 adsorption/desorption isotherm of UB, CB, and AB.

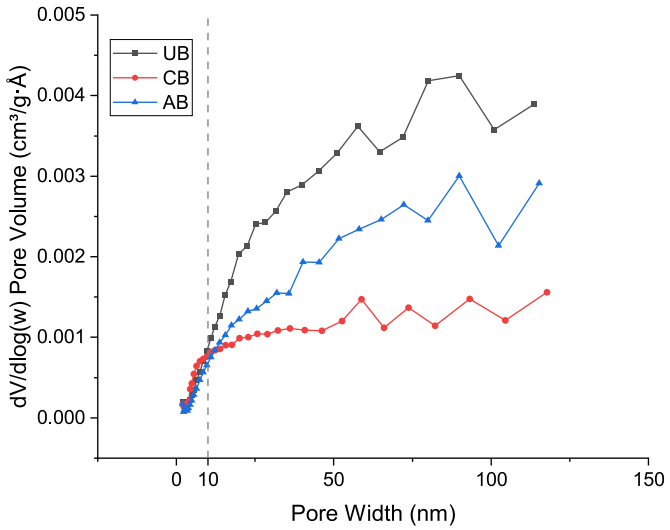

Fig. 6. Differential pore width distribution curves of UB, CB, and AB.

specific surface area. Besides, CB and AB show significantly different surface morphology compared to UB, presenting a loose out-layer enriched with calcium carbonates. These changes dramatically influence the marco-mechanical strength and ITZ properties, as elaborated in the following sections.

3.2. Compressive strength of BOF slag mortars

Fig. 8 illustrates the compressive strength of all mortars after 28 days of curing. The compressive strength of UB, CB, and AB specimens are 31.6 %, 50.0 %, and 77.6 % (on average of values at varying TPC dosages), higher than NS references, respectively. All pure BOF slag-based mortars exhibit higher compressive strength than NS reference specimens. This is to be expected, as in pure BOF slag-based mortars, since both the binder and the aggregate are BOF slag that can be activated by TPC, the BOF slag aggregate (boundary) may also react to a certain extent, contributing to a stronger binding of binder/aggregate. It is also possible that not only can high-stiffness BOF slag aggregate help distribute stress more evenly, but the close stiffness of the BOF slag aggregate and binder also makes the pure BOF slag-based mortar more homogeneous overall [81]. Furthermore, mortars with treated BOF slag aggregates, especially AB, present more satisfying results than the UB reference. This result indicates that the interface BOF slag binder/BOF slag aggregate gets reinforced further after BOF slag aggregate treatments (especially autoclaving). It could be verified by the characterization results of BOF slag aggregate treatments: carbonation and autoclaving modify the relatively blank surface into a product-rich surface, thus generating a more robust aggregate/binder interlocking. Additionally, the compressive strength of all specimens increases with TPC dosages, which differs from the results of TPC-activated pure BOF slag-based pastes, where pastes activated by the lower dosage of TPC perform better [2]. The difference in compressive strength performance at varying TPC dosages between pure paste and mortar may be attributed to the enhancement of the ITZ microstructure within the mortar at higher TPC dosage, which offsets or even compensates for the disadvantages of higher TPC dosage, such as higher cracking rates or lower C_2S hydration degree [2].

3.3. Leaching properties of BOF slag mortars

Heavy metal ions such as vanadium (V) and chromium (Cr) are typically embedded in the hydraulically active phases (C_2S and brownmillerite) in BOF slag [16,82,83]. They may be released during the hydration process of BOF slag and the actual service of BOF

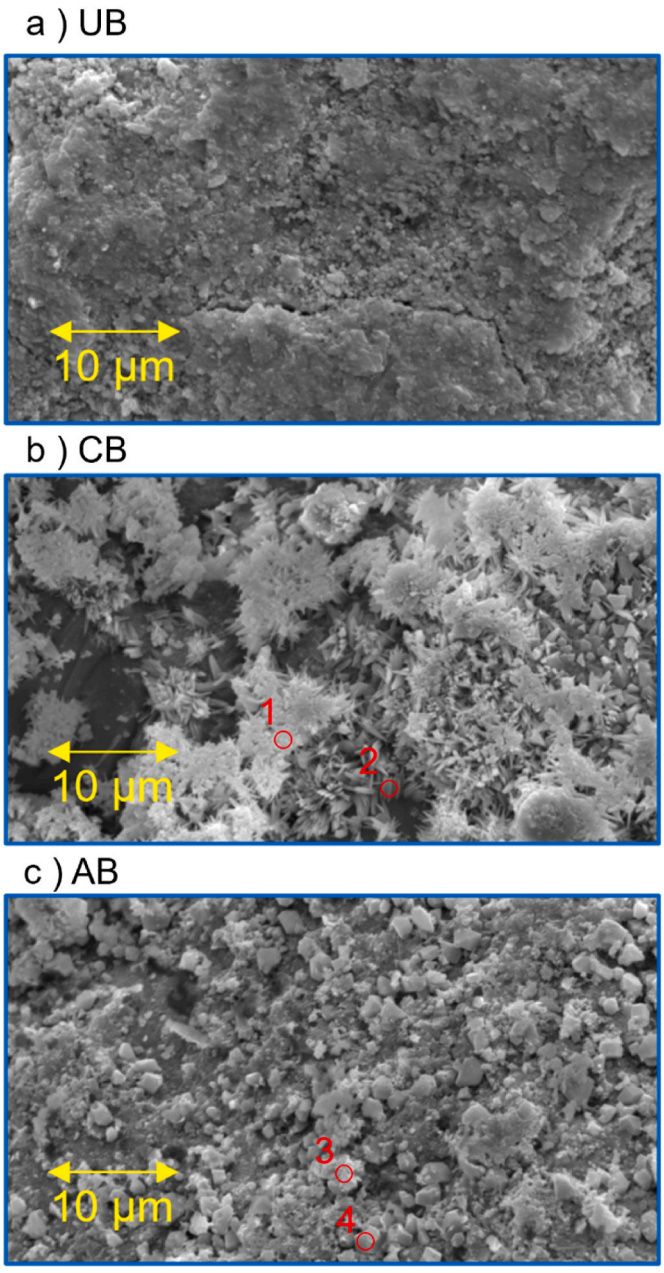

Fig. 7. SEM-SE images of BOF slag aggregates surface.

Table 5
Chemical compositions (at.%) of reaction products on CB and AB aggregates.

Position	Ca	Si	O	Fe
1	22.5	2.7	72.9	1.8
2	20.1	2.0	76.2	1.8
3	23.0	1.6	74.1	1.3
4	22.6	1.1	75.0	1.2

slag-based building materials, a potential risk to the environment [2,84,85]. Meanwhile, the effect of the introduced BOF slag aggregates on the leaching behavior should be clarified. For this reason, leaching values for all mortars were determined after 28 days of hydration through the one-stage leaching test, as shown in Table 6 [58]. Legal limits from the Dutch Soil Quality Decree (DSQD) are also given [86].

The leaching of V and Cr from all samples is below the legal limit, according to the Dutch Soil Quality Decree (DSQD) [86]. Hence, the risk

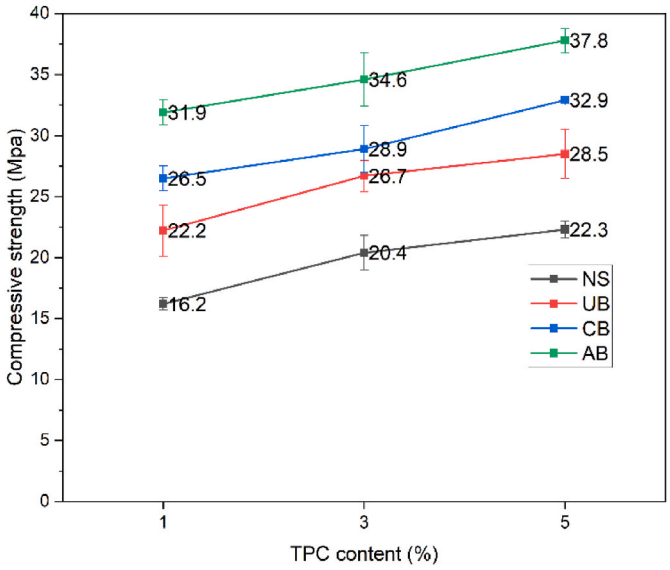

Fig. 8. Compressive strength of mortars after 28 days of hydration.

Table 6
Leaching[a] of TPC-activated BOF slag mortars and legal values from the DSQD.

Sample	Cr	V
	mg/Kg	mg/Kg
Unshaped material (DSQD)	0.63	1.80
NS1	0.06	0.04
NS3	0.06	0.12
NS5	0.09	0.23
UB1	0.04	0.07
UB3	0.06	0.10
UB5	0.07	0.18
AB1	0.02	0.06
AB3	0.04	0.08
AB5	0.08	0.17
CB1	0.04	0.12
CB3	0.07	0.23
CB5	0.09	0.37

[a] Elements under detection threshold: As, Cd, Co, Cu, Ni, Pb, Sb, Se, Zn, Ba, Mo.

of leaching is limited for TPC-activated BOF slag mortars, regardless of the aggregate types incorporated. Specifically, comparing the leaching values of UB and NS references, it can be concluded that usage of BOF slag aggregate does not increase the leaching values. Regarding the treatment influences, BOF slag aggregate carbonation increases the V leaching values of BOF slag mortars. Since V is mainly incorporated into C_2S, it can be inferred that after carbonation, the C_2S within BOF slag aggregate dissolves obviously and increases the V leaching [85].

The effects of TPC concentrations are apparent. Higher TPC dosages facilitate the leaching of V and Cr within all mortars, although the effect is limited for Cr and much more pronounced for V. The citrate ions act as ligands (complexing agents) for V and Cr, forming soluble V-citrate or Cr-citrate complexes [15,87]. This phenomenon could reduce the possibility of V and Cr immobilizing within stable hydration products at higher TPC concentrations, such as siliceous hydrogarnet and C-S-H gel [88,89].

3.4. ITZ properties

ITZ originates from the "wall" effect, the physical packing of unhydrated binder particles around aggregate grains that are several orders of magnitude larger in size [37]. As shown in Fig. 9, the much larger solid aggregate works like a "wall" and cuts through randomly distributed binder grains if it is put into the cluster of binder particles, which will not actually happen when aggregate is mixed with binder particles. Thus, the random distribution of binder grains in different sizes is disrupted by the aggregate. Binder grains rearrange, and a zone lacking large particles and dominated by small particles near the aggregate boundary generates [36,37,41,42,63]. As discussed in the introduction, ITZ is generally a critical weak region where cracks initiate and propagate. Hence, the ITZ of pure BOF slag-based mortars was characterized and then analyzed in detail to investigate the effects of carbonation and autoclaving of BOF slag aggregate.

3.4.1. ITZ determination

In this research, the BOF slag aggregate size is 1–2 mm, while 90 % of BOF slag binder grains are below 27 μm (as shown in Fig. 1), which is the origin of the ITZ within pure BOF slag-based mortars. The ITZ in actual pure BOF slag-based mortars is shown in Fig. 10: only small BOF slag binder grains are present in the area close to the edge of the BOF slag aggregate, and large BOF slag binder particles are only found farther away.

The ITZ range was determined by quantitative calculation based on the method described in Section 2.4 and the internal MATLAB batch process code. Mean volume fractions of three constituents: pores, hydration products (HP), and unreacted particles (UP), were calculated based on clipped strips from BSE images. These values are anchored at the farther edge of each strip from the aggregate, as shown in Fig. 11. For most mortars, noticeable constituent content gradients between the vicinity of the aggregate edge and further away areas can be observed at each TPC dosage. Even though the effects of BOF slag aggregate

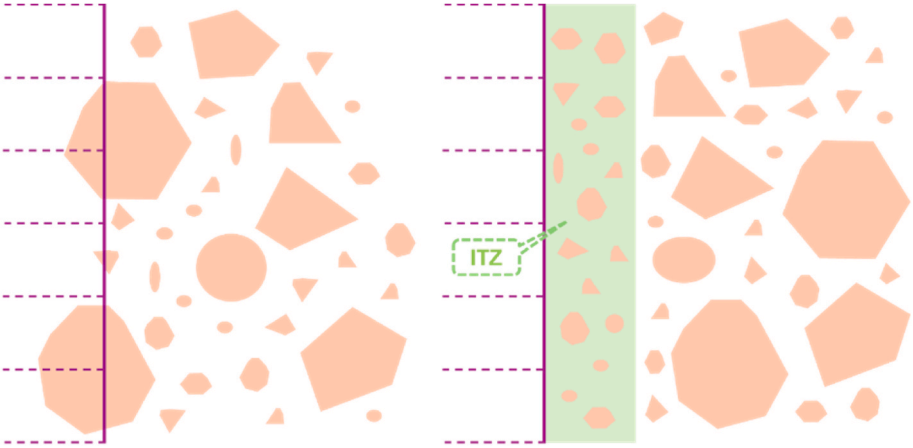

Fig. 9. A schematic diagram of the "wall" effect and the origin of ITZ.

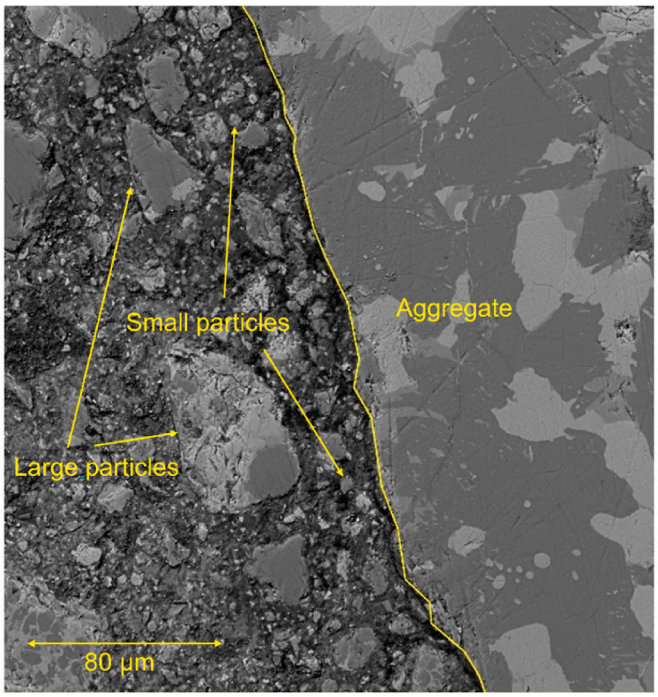

Fig. 10. Distribution of BOF slag binder particles within the periphery of BOF slag aggregate surface.

treatments are not evident at all TPC dosages, it could be easily observed that at 5 wt% of TPC, CB and AB mortars display a more refined microstructure (less unreacted particles, lower porosity, and more hydration products) than the UB and NS references in the general binder region (including both ITZ and matrix). The effects of TPC dosages are not easily discernible, although the microstructures of the general binder region around the binder/aggregate interface seem to improve at higher TPC dosages.

Fig. 11 gives the mean volume fractions of three constituents (pores, hydration products, and unreacted particles) from 30 BSE graphs (consisting of 12 clipped strips each) for each sample. To verify the statistical significance of these data, the coefficients of variation (COV, a ratio of the standard deviation to the mean, and multiplied by 100) of constituent compositions from 30 BSE graphs of each sample were calculated [42,90]. COV values for all samples are illustrated in Fig. 12 as a function of distance from the aggregate edge. It is easily observed that COVs of porosity show dramatically high values, up to 175 %, and fluctuate significantly, indicating statistical variation of porosities within BSE images taken in different locations within the same sample. The high variation could be attributed to the complex components categorized and calculated as ''pores'': capillary pores, microcracks, and trapped air voids. This complexity results in evident variation and unpredictability of calculated porosity from different locations (BSE images) in a mortar. Besides, the relatively low w/b ratio and percentage of pores also exacerbate the situation. Such variation is intrinsic to cementitious binding materials and inevitable [90]. In comparison, COVs for hydration products and unreacted particles only vary from around 3 %–37 % within all samples, which exhibits low variability of volume fractions for unreacted particles and hydration products calculated from different regions. Due to this, the mean volume fractions of unreacted particles and hydration products can describe the interface features at a certain distance from the aggregate boundary with statistical significance. Also, the gradients of unreacted particles and hydration products fit well with the origin of ITZ, the "wall" effect. Hence, it is reasonable to utilize the gradient of mean volume fractions of unreacted particles and hydration products to determine the ITZ boundary.

A quantitative difference analysis was conducted to more intuitively and clearly identify the changes of constituent volume fractions along outward successive strips from the aggregate surface [42]. The difference values for both unreacted particles (D_{UP}) and hydration products (D_{HP}) are expressed below:

$$D_{UP} = \frac{|UP_i - UP_1|}{UP_1} \times 100\% \quad (1)$$

$$D_{HP} = \frac{|HP_j - HP_1|}{HP_1} \times 100\% \quad (2)$$

Here, UP_1 refers to the volume percent of unreacted particles in the strip closest to the aggregate surface, and UP_i denotes the volume fraction of unreacted particles within the ith strip; HP_1 means the volume fraction of hydration products in the strip nearest to the aggregate surface, and HP_j is the volume fraction of hydration products within the jth strip.

Difference curves for all specimens are presented in Fig. 13. For the NS1 mortar, the D_{UP} has a steep rise from 0 % to 52 %, and the D_{HP} has a gentle ascent from 0 % to 12 % as the distance increases to 40 μm. Then, they remain relatively steady in the region beyond 40 μm. This phenomenon illustrates a noticeable difference in the binder microstructure between the periphery of the aggregate surface and the farther areas. The region around the aggregate with a high gradient of microstructural constituents could be defined as the ITZ, and the more outlying areas (with relatively stable microstructural constituents) could be considered as the matrix [35–37,39,42]. A different pattern is observed for the NS3 mortar, as shown in Fig. 13b. The D_{UP} increases to 35 % at 15 μm and then reduces to 22 % at 20 μm. Then, it rises to 47 % at 35 μm and starts fluctuating around the value. The D_{HP} exhibits a slight upward trend from the closest to the farthest strip in general. The ITZ boundary is determined at 35 μm here. NS5 shows a similar trend as NS1. Its ITZ boundary is defined as 45 μm.

According to Fig. 13d, for the UB1, the D_{UP} grows from 0 % to 51 % between 5 μm and 35 μm. Then, it stays relatively stable with a slight upward trend from 35 μm to the farthest measured zone. The D_{HP} profile demonstrates a similar trend. The boundary between ITZ and matrix is determined at 35 μm here. For the UB3 specimen, according to Fig. 13e, the D_{UP} and D_{HP} increase from 0 % to 25 % and from 0 % to 7 %, respectively, with distances from 5 μm to 15 μm and then they fluctuate around these two values with increasing distance from the grain. The boundary is defined at 15 μm. For UB5, the D_{UP} increases significantly from 0 to 29 % between 0 and 25 μm, then shows a gentle increase. D_{HP} presents a similar trend, peaking around 12 % at 15 μm, then slightly rising. The ITZ border is determined at 25 μm. In the same way, the ITZ width for CB1, CB3, CB5, AB1, AB3, and AB5 are defined as 40 μm, 30 μm, 25 μm, 30 μm, 15 μm, and 20 μm respectively. NS mortars have ITZ thicknesses ranging from 35 to 45 μm. In comparison, pure BOF slag-based mortars generally show thinner ITZ, especially AB specimens with a much lower ITZ thickness ranging from 15 to 30 μm. It needs to be noted that, according to Fig. 13, the boundary between ITZ and binder matrix within some mortars is relatively vague and depends on the constituent focused on (unreacted particles or hydration products). The boundary between ITZ and matrix is not a clear edge but a gradual transition, similar to Portland cement and alkaline-activated binder systems [37,42].

Another critical feature that occurs within the ITZ region is microcracking. The more porous or weaker microstructures facilitate or even promote the initiation and propagation of microcracks, thus providing a fast channel for the penetration of water and destructive ions [41,91,92]. Representative BSE images (at 1000 × magnification) of the aggregate interfacial regions within all mortars are presented in Fig. 14, demonstrating microcracks around the aggregate boundary. The microcracks could be easily identified as bond or matrix cracks [42,93]. Bond cracks mean cracks that appear along the edge of the aggregate, as shown in Fig. 14a, and matrix cracks refer to the microcracks existing within the binder matrix, as shown in Fig. 14c. As can be seen from

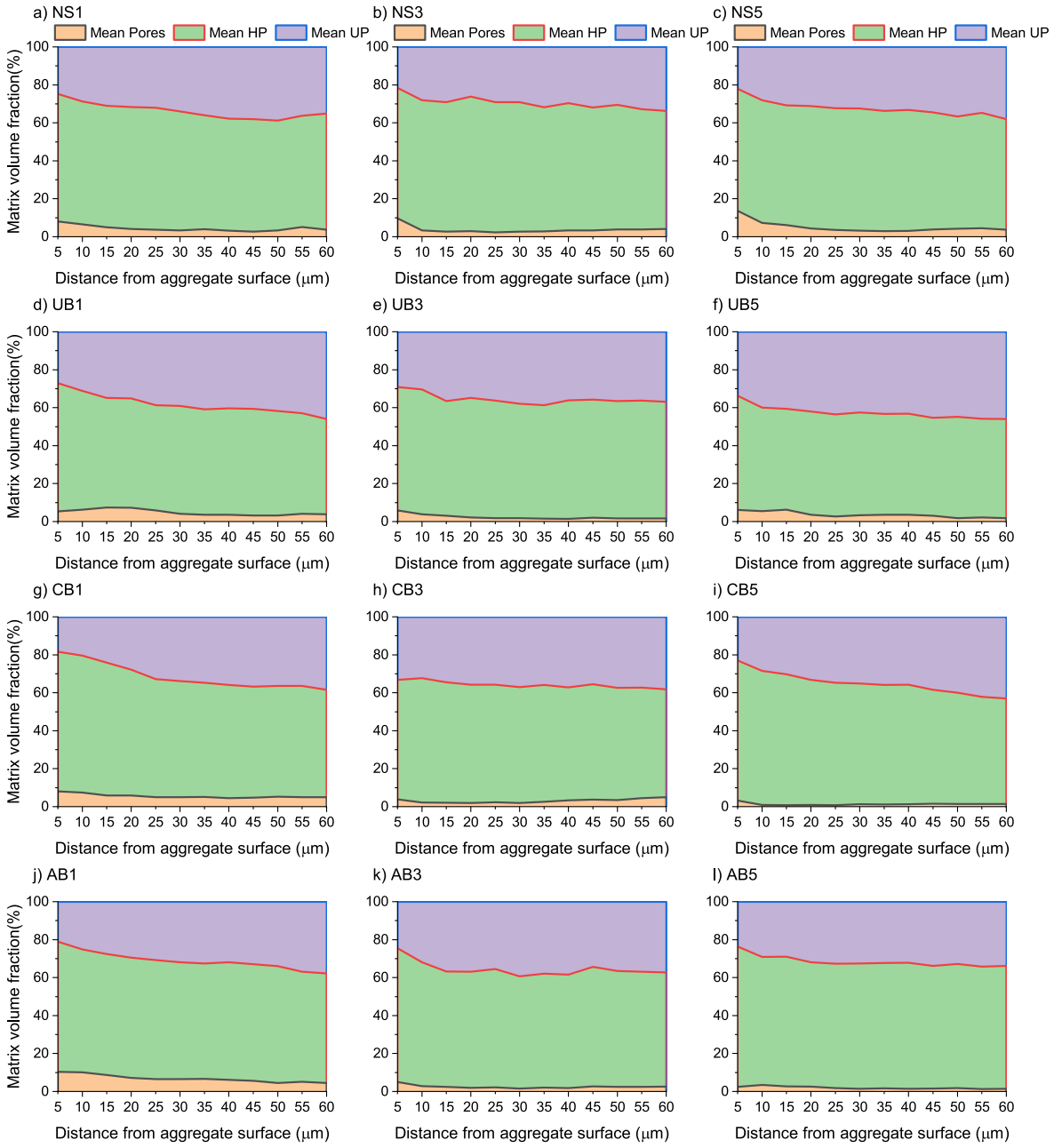

Fig. 11. Constituent compositions of the binder around the aggregate edge.

Fig. 14a–c, NS1 only shows bond cracks, while matrix cracks also initiate and develop in NS3 and NS5. In comparison, only matrix cracks are present within pure BOF slag-based mortars at all TPC dosages, which indicates a more robust aggregate/binder interface. Similar to the analysis of compressive strength, the possible edge hydration of BOF slag aggregate may partially contribute to the enhanced aggregate/-binder interface (i.e., without bond cracks). More frequent and broader matrix cracks develop within mortars at high TPC contents, regardless of the aggregate types. Such a phenomenon is possibly due to the incorporation of K (from activator, TPC). As K is highly soluble, it is most likely embedded in the gels, which may cause the incompatibility between K-rich and K-depleted gels, causing internal stresses and strains in the matrix, thus leading to more matrix cracks in the K-enriched area [2,94,95].

Overall, by quantitative constituent analysis of 30 BSE images for each mortar sample, it can be concluded that pure BOF slag-based mortars, especially specimens with AB aggregate, present a narrower ITZ than NS references. Moreover, no bond cracks appear within pure BOF slag-based mortars at any TPC dosages, indicating a more robust aggregate/binder interface. These could be the reason for the better compressive strength of pure BOF slag mortars, especially AB specimens with autoclaved BOF slag aggregate.

3.4.2. *Comparative analysis of ITZ/matrix*

The deficit of large binder grains within the ITZ also means a relatively lower binder content compared with the binder matrix. This characteristic initially induces a higher local water/binder ratio and a higher local activator/binder ratio, which causes the difference in properties between ITZ and the binder matrix during hydration. According to the determined ITZ widths (as shown in Fig. 13) and an in-house MATLAB batch process code (based on the extended ''OTSU'' algorithm described in Section 2.4.3), the content of unreacted particles, hydration products, and pores was calculated within ITZ and matrix, respectively, to analyze the influence of BOF slag aggregate carbonation

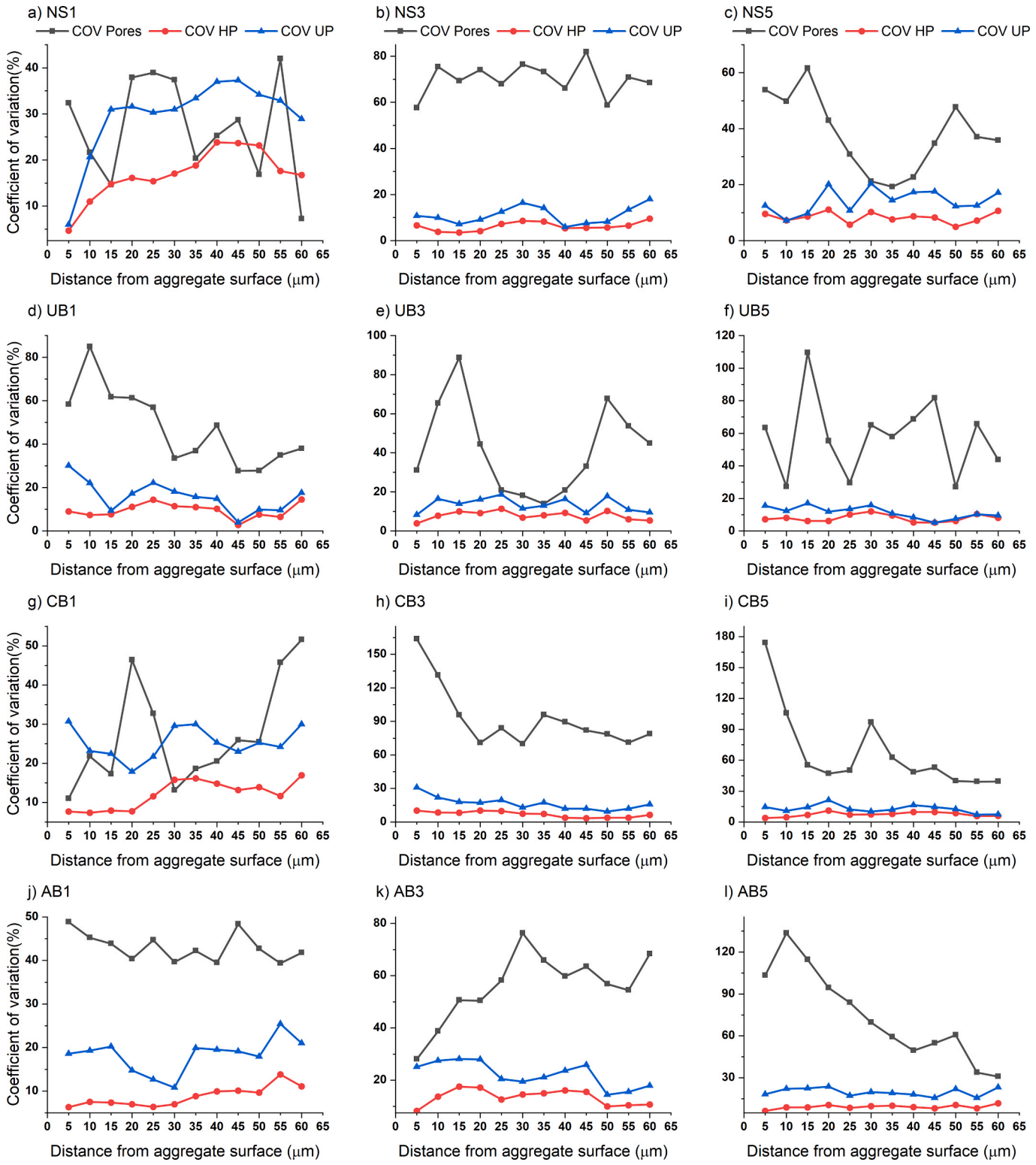

Fig. 12. Coefficients of variation of constituent compositions against distance from the aggregate edge.

and autoclaving.

Fig. 15 shows unreacted particle contents within the ITZ and the bulk matrix for all samples. It is clear that even after 28 days of hydration, there are fewer unreacted particles in the ITZ region than in the binder matrix for all specimens. Volume fractions of unreacted particles within UB references are higher than those in NS references, both in the ITZ and matrix regions. The difference (average at three TPC dosages) is 11 % and 12 % in the ITZ and the matrix, respectively. This situation could be due to the higher water/binder and activator/binder ratios in the general binder region of NS references, which induce faster consumption of unreacted particles. Because in the NS references, the aggregate itself does not react. CB and AB mortars have obviously lower contents of unreacted particles in general, both in the ITZ and matrix areas, compared with those in the UB references. For example, AB specimens have 26 and 32 vol% (on average of different TPC dosages) unreacted particles in the ITZ and matrix, respectively. In contrast, UB references

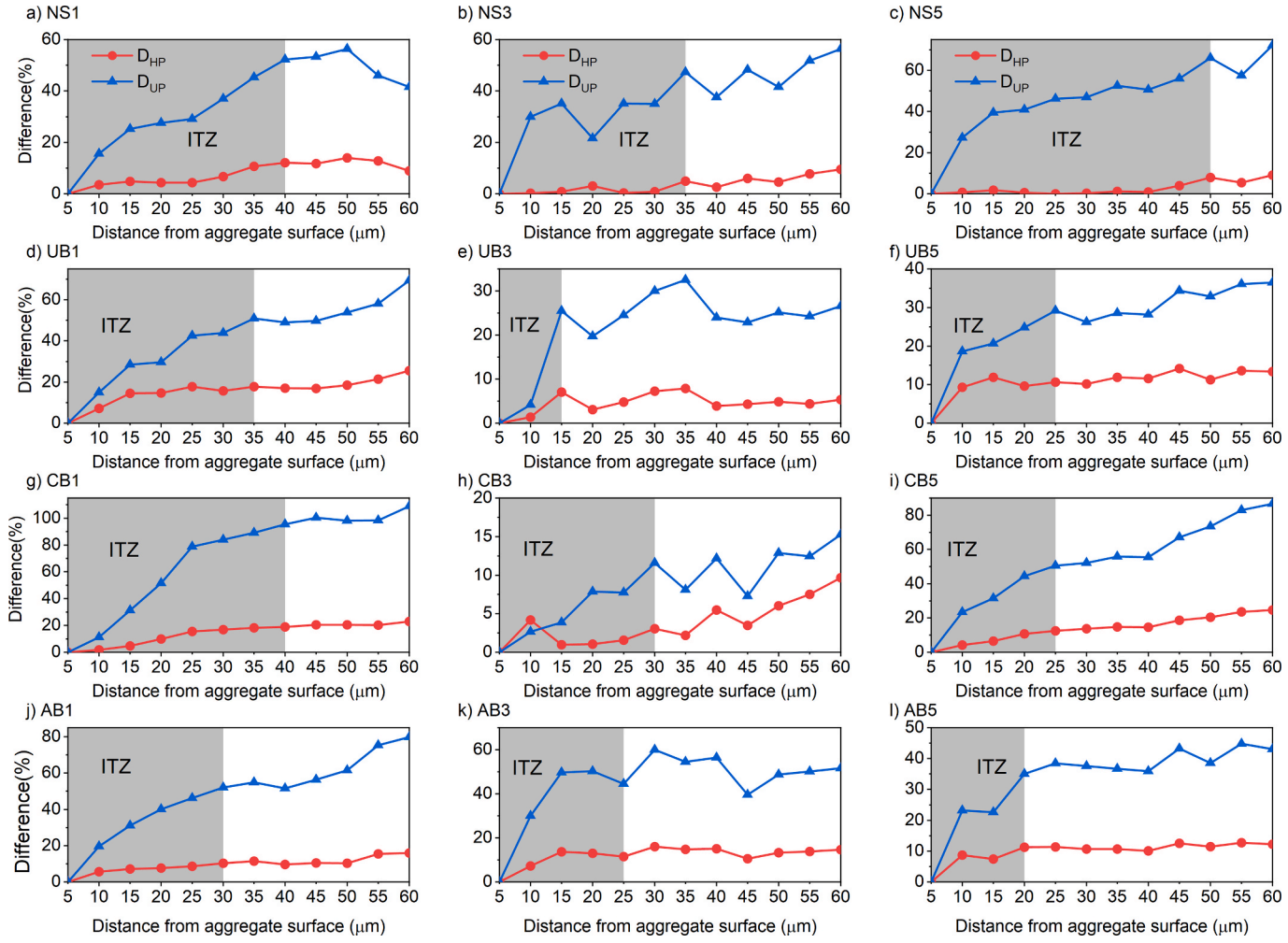

Fig. 13. Difference of unreacted particles and hydration products between the first strip and outward successive strips.

have 36 and 42 vol% (average at different TPC dosages) of unreacted particles in the ITZ and matrix, respectively. Carbonation and autoclaving of BOF slag aggregate appear to benefit the hydration of unreacted particles in the integral binder region. One possible explanation is that, for CB and AB, the reactive mineral phases on the surface of the aggregate have already reacted, or at least partially. Therefore, the carbonated or autoclaved BOF slag aggregate, CB and AB, do not consume as much activator and water as UB. Thus, in the whole binder area, the unreacted particles are consumed more fully, similar to the situation of NS references. However, CB and AB aggregate (boundary) may still react to a certain extent when in contact with water and the activator. Thus, they still have more unreacted particles in the general binder region than NS references. For example, CB specimens have 12 % and 17 % more unreacted particles in the ITZ and matrix, respectively, compared with those of NS references. The treatments have no apparent effects on the ITZ/matrix difference. Also, no clear trends could be observed within each specimen at varying TPC dosages.

Fig. 16 presents the hydration product volume fractions within ITZ and binder matrix from all specimens at different TPC dosages. It is clear that after 28 days, hydration products are more abundant within the ITZ than in the matrix for all specimens. UB mortars have 11 vol% (average of different TPC dosages) fewer hydration products than NS references in both the ITZ and the matrix, respectively, which is consistent with the unreacted particles trend and could again be attributed to the higher water/binder and activator/binder ratios in binder region within NS reference specimens. At the same time, the contents of hydration products within CB and AB samples, either in ITZ or the bulk matrix, are higher than those in UB references. For example, AB specimens have 69 and 65 vol% (average of different TPC dosages) of hydration products in the ITZ and matrix, respectively. In comparison, UB references have only 59 and 56 vol% (average of different TPC dosages) of hydration products in the ITZ and matrix, respectively. Therefore, aggregate carbonation and autoclaving treatments facilitate the formation of hydration products within the general binder area, which should also be part of the reason for the better compressive strength of CB and AB mortars than UB references. This facilitation effect can also be attributed to the same reason as the promoted consumption of unreacted particles. The treated reaction product-rich aggregate surface may also offer more nucleation sites, thus being beneficial for the generation of hydration products within the whole binder region and also a stronger biner/aggregate bonding. BOF slag aggregate carbonation or autoclaving treatment demonstrated no statistically significant effect on the volume fraction difference of hydration products within the ITZ/matrix, resembling the situation for unreacted particles. Similarly, the impact of TPC dosages on this difference is also not noticeable.

The EDS spot analysis was conducted in the ITZ and the matrix to gain a deeper understanding of the compositional difference of hydration products within these two areas. However, it is hard to conclude some significant trends except the EDS results of K (mainly from the activator). Thus, only the EDS results of K are presented and analyzed. As can be seen from Fig. 17, there is no clear trend of distinction for K distribution between the ITZ and the matrix. Considering the treatment influences, AB samples have the highest K atomic percentage within all specimens at each TPC dosage. For example, the K atomic percentage is

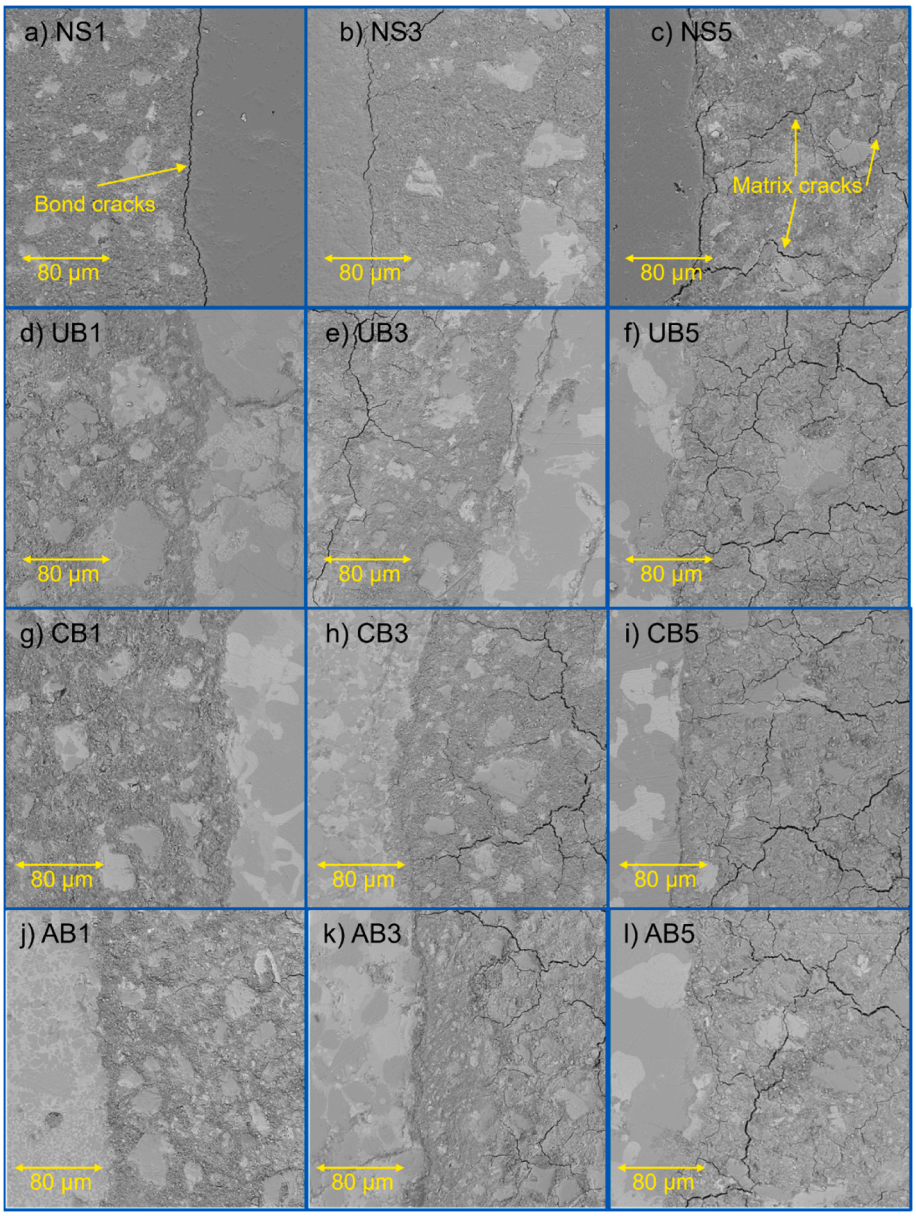

Fig. 14. BSE images of interfaces near aggregate boundary within all samples.

10 at.% in the general binder region (average of the ITZ and the matrix) of AB5, which is 71 % and 49 % higher compared with that of CB5 and UB5, respectively. As analyzed above, K is highly soluble and most likely embedded in gel products. The higher atomic percentage of K in AB samples may indicate more gel products, which may also benefit their strength performance. Within each kind of sample, the atomic percentage of K increases with the growth of TPC concentration either in ITZ or matrix, which is as expected.

Porosity is another crucial microstructural characteristic that affects the ITZ properties. However, as presented in Fig. 12, the variation of porosity data from different locations within one sample is very high. Thus, inferring reliable and valuable conclusions from the porosity data within the ITZ/matrix is difficult since the data has a high deviation (see Fig. 18).

4. Conclusion

In this research, pure BOF slag-based mortars were proposed and investigated with tri-potassium citrate-activated BOF slag as binder and carbonated and autoclaved BOF slag as fine aggregates. Mortars utilizing natural sand and untreated BOF slag as fine aggregate were set as the references. Effects of carbonation and autoclaving on BOF slag aggregate were characterized first. The influence of aggregate carbonation and autoclaving on the compressive strength and leaching properties of pure BOF slag-based mortars was investigated. Finally, the effects of these two treatments on the ITZ properties were analyzed in depth. Based on the above investigations, conclusions are drawn as follows:

- Both carbonation and autoclaving treatments reduce the free CaO, promote the formation of $CaCO_3$, and decrease the amorphous content. Pores of BOF slag aggregate are also filled and refined, most likely by calcium carbonates. Besides, the two treatments alter the surface morphology of BOF slag aggregate from relatively smooth to irregular products-enriched out-layer.
- Pure BOF slag-based mortars exhibit higher compressive strength than the NS references, which reflects stronger bonding and interlocking between binder and aggregate that is possibly attributed to the BOF slag aggregate (periphery) hydration and the pressure

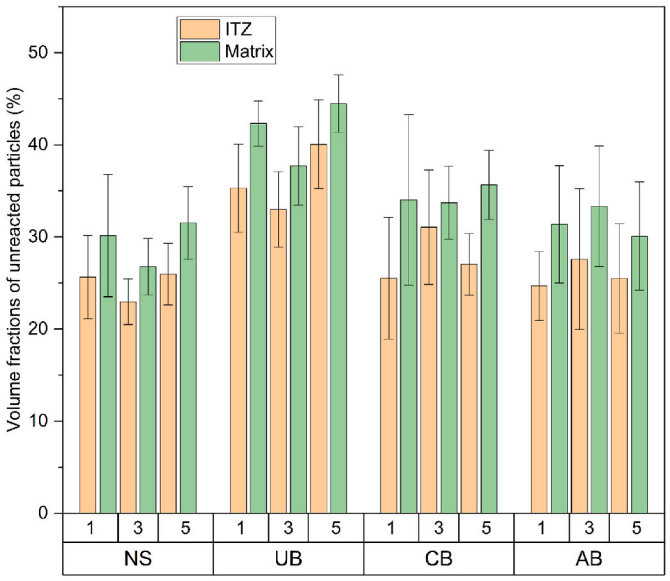

Fig. 15. Unreacted particle contents in ITZ vs. matrix at varying TPC dosages.

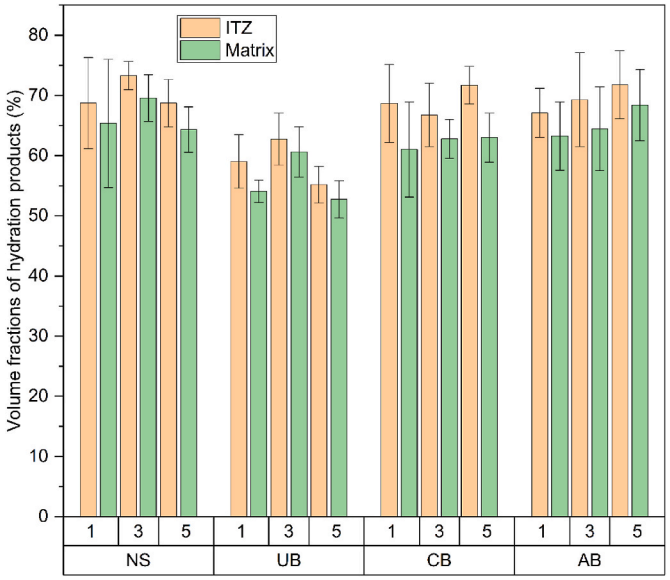

Fig. 16. Hydration product contents in ITZ vs. matrix at varying TPC dosages.

distribution capacity due to its high stiffness. BOF slag aggregate treatments, especially autoclaving, enhance the compressive strength of pure BOF slag-based mortars, which may benefit from the surface morphology change and resulting stronger aggregate/binder interlocking.

- Within heavy metal cations categorized by the Dutch Soil Quality Decree, only V and Cr could be detected in the leaching test, and the leaching risk is low for all mortars, regardless of aggregate type. The usage of BOF slag aggregate does not increase the leaching risk. Moreover, only carbonation increases the V leaching values of BOF slag mortars, which could be attributed to the reaction of (amorphous) C_2S that incorporates the V. Besides, higher TPC dosages induce the higher leaching values of V and Cr within all mortars, which could be ascribed to the enhanced dissolution of hydraulically reactive phases and resulting in the formation of soluble V-citrate or Cr-citrate complexes, thus lowering their immobilization within hydration products.

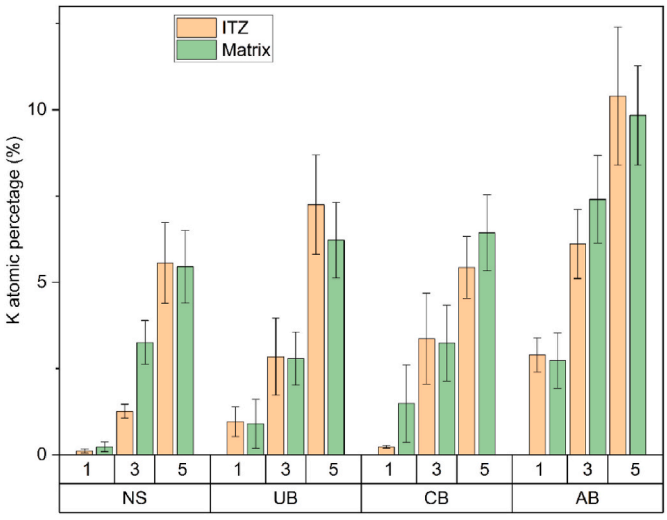

Fig. 17. Comparison of K atomic concentration within ITZ and matrix.

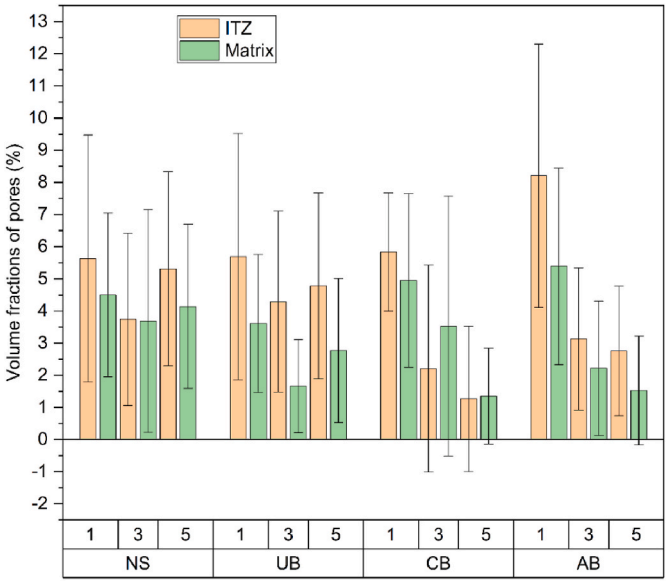

Fig. 18. Pore contents (porosities) in ITZ vs. matrix at varying TPC dosages.

- Pure BOF slag-based mortars, especially AB specimens, present narrower ITZ than the NS references. Moreover, no bond cracks appear within pure BOF slag-based mortars at any TPC dosages. These indicate a more robust aggregate/binder interface within pure BOF slag-based mortars, especially AB samples, and could also be a (partial) reason for the better compressive strength.
- CB and AB mortars contain fewer unreacted particles and more hydration products in both ITZ and matrix regions than the UB references, which could be attributed to the varying hydration degrees of the aggregate itself and the different consumption of the activator and water related to that. The treated product-rich aggregate surface with more nucleation sites may also benefit the hydration product generation.

Looking forward, the long-term volume stability of TPC-activated BOF slag binder with different initial free CaO contents is a topic worthy of in-depth discussion. Besides, as described in Section 2.4.1, it is pretty challenging to determine the boundary of aggregate/binder automatically, especially in this research where both aggregate and binder are BOF slag. Hence, we applied the artificial method to

determine the boundary between the binder and the aggregate. However, this method is very time-intensive. Research on more objective and automated methods is of great significance, especially in studies like this where the binder and aggregate are the same material and the aggregate has many different internal phases (and the aggregate may also react). Training an algorithm (whether based on grayscale differences or some physical geometric features) to accurately distinguish the binder and aggregate would be advantageous.

CRediT authorship contribution statement

Zhihan Jiang: Writing – original draft, Methodology, Investigation, Formal analysis, Data curation, Conceptualization. **Jonathan Zepper:** Writing – review & editing, Methodology, Investigation, Data curation. **Xuan Ling:** Writing – review & editing, Methodology, Investigation, Data curation. **Katrin Schollbach:** Writing – review & editing, Supervision, Conceptualization. **H.J.H. Brouwers:** Writing – review & editing, Supervision, Conceptualization.

Declaration of competing interest

The authors declare that they have no known competing financial interests or personal relationships that could have appeared to influence the work reported in this paper.

Data availability

Data will be made available on request.

Acknowledgments

This work was supported by the China Scholarship Council (fund No. 201906950015, No. 202006950032). We also want to express our sincere gratitude to Anneke Delsing for assisting with the ICP-AES tests. The support of the research laboratories of Tata Steel Netherlands is acknowledged for facilitating the analysis and providing the raw materials.

References

[1] Y. Jiang, T.C. Ling, C. Shi, S.Y. Pan, Characteristics of steel slags and their use in cement and concrete—a review, Resour. Conserv. Recycl. 136 (2018) 187–197, https://doi.org/10.1016/j.resconrec.2018.04.023.
[2] A.M. Kaja, K. Schollbach, S. Melzer, S.R. van der Laan, H.J.H. Brouwers, Q. Yu, Hydration of potassium citrate-activated BOF slag, Cement Concr. Res. 140 (2021), https://doi.org/10.1016/j.cemconres.2020.106291.
[3] B. Pang, Z. Zhou, P. Hou, P. Du, L. Zhang, H. Xu, Autogenous and engineered healing mechanisms of carbonated steel slag aggregate in concrete, Construct. Build. Mater. 107 (2016) 191–202, https://doi.org/10.1016/j.conbuildmat.2015.12.191.
[4] F. Han, Z. Zhang, Properties of 5-year-old concrete containing steel slag powder, Powder Technol. 334 (2018) 27–35, https://doi.org/10.1016/J.POWTEC.2018.04.054.
[5] Q. Wang, P. Yan, J. Yang, B. Zhang, Influence of steel slag on mechanical properties and durability of concrete, Construct. Build. Mater. 47 (2013) 1414–1420, https://doi.org/10.1016/J.CONBUILDMAT.2013.06.044.
[6] World Steel Statistics, 2022. https://worldsteel.org/data/world-steel-in-figures-2023/#world-crude-steel-production-%3Cbr%3E1950-to-2022.
[7] F. Han, Z. Zhang, D. Wang, P. Yan, Hydration heat evolution and kinetics of blended cement containing steel slag at different temperatures, Thermochim. Acta 605 (2015) 43–51, https://doi.org/10.1016/J.TCA.2015.02.018.
[8] G. Wang, Y. Wang, Z. Gao, Use of steel slag as a granular material: volume expansion prediction and usability criteria, J. Hazard Mater. 184 (2010) 555–560, https://doi.org/10.1016/j.jhazmat.2010.08.071.
[9] A.S. Brand, J.R. Roesler, Steel furnace slag aggregate expansion and hardened concrete properties, Cem. Concr. Compos. 60 (2015) 1–9, https://doi.org/10.1016/j.cemconcomp.2015.04.006.
[10] N. Palankar, A.U. Ravi Shankar, B.M. Mithun, Durability studies on eco-friendly concrete mixes incorporating steel slag as coarse aggregates, J. Clean. Prod. 129 (2016) 437–448, https://doi.org/10.1016/j.jclepro.2016.04.033.
[11] M. Bodor, R.M. Santos, G. Cristea, M. Salman, Ö. Cizer, R.I. Iacobescu, Y. W. Chiang, K. Van Balen, M. Vlad, T. Van Gerven, Laboratory investigation of carbonated BOF slag used as partial replacement of natural aggregate in cement mortars, Cem. Concr. Compos. 65 (2016) 55–66, https://doi.org/10.1016/j.cemconcomp.2015.10.002.
[12] Q. Wang, D. Wang, S. Zhuang, The soundness of steel slag with different free CaO and MgO contents, Construct. Build. Mater. 151 (2017) 138–146, https://doi.org/10.1016/j.conbuildmat.2017.06.077.
[13] Q. Dong, G. Wang, X. Chen, J. Tan, X. Gu, Recycling of steel slag aggregate in portland cement concrete: an overview, J. Clean. Prod. 282 (2021) 124447, https://doi.org/10.1016/j.jclepro.2020.124447.
[14] G. Wang, Y. Wang, Z. Gao, Use of steel slag as a granular material: volume expansion prediction and usability criteria, J. Hazard Mater. 184 (2010) 555–560, https://doi.org/10.1016/J.JHAZMAT.2010.08.071.
[15] A.M. Kaja, K. Schollbach, S. Melzer, S.R. van der Laan, H.J.H. Brouwers, Q. Yu, Hydration of potassium citrate-activated BOF slag, Cement Concr. Res. 140 (2021) 106291, https://doi.org/10.1016/j.cemconres.2020.106291.
[16] W.F. Santos, K. Schollbach, S. Melzer, S.R. van der Laan, H.J.H. Brouwers, Quantitative analysis and phase assemblage of basic oxygen furnace slag hydration, J. Hazard Mater. 450 (2023) 131029, https://doi.org/10.1016/j.jhazmat.2023.131029.
[17] W. Franco Santos, J.J. Botterweg, S. Chaves Figueiredo, K. Schollbach, S. van der Laan, H.J.H. Brouwers, Sodium oxalate activation of basic oxygen furnace slag for building materials, Resour. Conserv. Recycl. 198 (2023) 107174, https://doi.org/10.1016/j.resconrec.2023.107174.
[18] L. De Windt, P. Chaurand, J. Rose, Kinetics of steel slag leaching: batch tests and modeling, Waste Manag. 31 (2011) 225–235, https://doi.org/10.1016/J.WASMAN.2010.05.018.
[19] S. Hu, H. Wang, G. Zhang, Q. Ding, Bonding and abrasion resistance of geopolymeric repair material made with steel slag, Cem. Concr. Compos. 30 (2008) 239–244, https://doi.org/10.1016/J.CEMCONCOMP.2007.04.004.
[20] Q. Wang, P. Yan, Hydration properties of basic oxygen furnace steel slag, Construct. Build. Mater. 24 (2010) 1134–1140, https://doi.org/10.1016/j.conbuildmat.2009.12.028.
[21] E. Belhadj, C. Diliberto, A. Lecomte, Characterization and activation of basic oxygen furnace slag, Cem. Concr. Compos. 34 (2012) 34–40, https://doi.org/10.1016/j.cemconcomp.2011.08.012.
[22] S. Kourounis, S. Tsivilis, P.E. Tsakiridis, G.D. Papadimitriou, Z. Tsibouki, Properties and hydration of blended cements with steelmaking slag, Cement Concr. Res. 37 (2007) 815–822, https://doi.org/10.1016/j.cemconres.2007.03.008.
[23] T.S. Zhang, F.T. Liu, S.Q. Liu, Z.H. Zhou, X. Cheng, Factors influencing the properties of a steel slag composite cement, Adv. Cement Res. 20 (2008) 145–150, https://doi.org/10.1680/ADCR.2008.20.4.145/ASSET/IMAGES/SMALL/ADCR20-145-F7.GIF.
[24] P.Y. Mahieux, J.E. Aubert, G. Escadeillas, Utilization of weathered basic oxygen furnace slag in the production of hydraulic road binders, Construct. Build. Mater. 23 (2009) 742–747, https://doi.org/10.1016/J.CONBUILDMAT.2008.02.015.
[25] J. Li, Q. Yu, J. Wei, T. Zhang, Structural characteristics and hydration kinetics of modified steel slag, Cement Concr. Res. 41 (2011) 324–329, https://doi.org/10.1016/J.CEMCONRES.2010.11.018.
[26] Z. Li, S. Zhao, X. Zhao, T. He, Cementitious property modification of basic oxygen furnace steel slag, Construct. Build. Mater. 48 (2013) 575–579, https://doi.org/10.1016/J.CONBUILDMAT.2013.07.068.
[27] Y. Lun, M. Zhou, X. Cai, F. Xu, Methods for Improving Volume Stability of Steel Slag as Fine Aggregate, twenty third ed., J. Wuhan Univ. Technol. Sci., 2008, pp. 737–742, https://doi.org/10.1007/s11595-007-5737-3.
[28] B. Pang, Z. Zhou, H. Xu, Utilization of carbonated and granulated steel slag aggregate in concrete, Construct. Build. Mater. 84 (2015) 454–467, https://doi.org/10.1016/J.CONBUILDMAT.2015.03.008.
[29] W.C. Wang, Feasibility of stabilizing expanding property of furnace slag by autoclave method, Construct. Build. Mater. 68 (2014) 552–557, https://doi.org/10.1016/j.conbuildmat.2014.06.082.
[30] İ. Yüksel, A Review of Steel Slag Usage in Construction Industry for Sustainable Development, Springer Netherlands, 2017, https://doi.org/10.1007/s10668-016-9759-x.
[31] T.C. Alex, G. Mucsi, T. Venugopalan, S. Kumar, BOF steel slag: critical Assessment and integrated approach for utilization, J. Sustain. Metall. 7 (2021) 1407–1424, https://doi.org/10.1007/S40831-021-00435-2/FIGURES/8.
[32] J. Liu, R. Guo, Applications of steel slag powder and steel slag aggregate in ultra-high performance concrete, Adv. Civ. Eng. 2018 (2018), https://doi.org/10.1155/2018/1426037.
[33] J.P. Ollivier, J.C. Maso, B. Bourdette, Interfacial transition zone in concrete, Adv. Cement Base Mater. 2 (1995) 30–38, https://doi.org/10.1016/1065-7355(95)90037-3.
[34] K.L. Scrivener, Backscattered electron imaging of cementitious microstructures: understanding and quantification, Cem. Concr. Compos. 26 (2004) 935–945, https://doi.org/10.1016/J.CEMCONCOMP.2004.02.029.
[35] A. Elsharief, M.D. Cohen, J. Olek, Influence of aggregate size, water cement ratio and age on the microstructure of the interfacial transition zone, Cement Concr. Res. 33 (2003) 1837–1849, https://doi.org/10.1016/S0008-8846(03)00205-9.
[36] W.K.W. Lee, J.S.J. Van Deventer, The interface between natural siliceous aggregates and geopolymers, Cement Concr. Res. 34 (2004) 195–206, https://doi.org/10.1016/S0008-8846(03)00250-3.
[37] K.L. Scrivener, A.K. Crumbie, P. Laugesen, The interfacial transition zone (ITZ) between cement paste and aggregate in concrete, Interface Sci. 12 (2004) 411–421, https://doi.org/10.1023/B:INTS.0000042339.92990.4c.
[38] Y. Gao, G. De Schutter, G. Ye, Z. Tan, K. Wu, The ITZ microstructure, thickness and porosity in blended cementitious composite: effects of curing age, water to binder

ratio and aggregate content, Composites, Part B 60 (2014) 1–13, https://doi.org/10.1016/j.compositesb.2013.12.021.
[39] R. San Nicolas, J.L. Provis, The interfacial transition zone in alkali-activated slag mortars, Front. Mater. 2 (2015) 70, https://doi.org/10.3389/fmats.2015.00070.
[40] A.S. Brand, J.R. Roesler, Bonding in cementitious materials with asphalt-coated particles: Part I – the interfacial transition zone, Construct. Build. Mater. 130 (2017) 171–181, https://doi.org/10.1016/j.conbuildmat.2016.10.019.
[41] A.S. Brand, J.R. Roesler, Interfacial transition zone of cement composites with steel furnace slag aggregates, Cem. Concr. Compos. 86 (2018) 117–129, https://doi.org/10.1016/j.cemconcomp.2017.11.012.
[42] G. Fang, M. Zhang, The evolution of interfacial transition zone in alkali-activated fly ash-slag concrete, Cement Concr. Res. 129 (2020) 105963, https://doi.org/10.1016/j.cemconres.2019.105963.
[43] D.P. Bentz, E.J. Garboczi, C.J. Haecker, O.M. Jensen, Effects of cement particle size distribution on performance properties of Portland cement-based materials, Cement Concr. Res. 29 (1999) 1663–1671, https://doi.org/10.1016/S0008-8846(99)00163-5.
[44] L. Holzer, R.J. Flatt, S.T. Erdoğan, J.W. Bullard, E.J. Garboczi, Shape comparison between 0.4–2.0 and 20–60 μm cement particles, J. Am. Ceram. Soc. 93 (2010) 1626–1633, https://doi.org/10.1111/J.1551-2916.2010.03654.X.
[45] British Standards Institution., Methods of testing cement. Part vol. 1, Determination of strength., (n.d.) 33. https://www.en-standard.eu/bs-en-196-1-2016-methods-of-testing-cement-determination-of-strength/(accessed July 25, 2023).
[46] D.P. Bentz, Influence of internal curing using lightweight aggregates on interfacial transition zone percolation and chloride ingress in mortars, Cem. Concr. Compos. 31 (2009) 285–289, https://doi.org/10.1016/j.cemconcomp.2009.03.001.
[47] Z. Wu, H.S. Wong, N.R. Buenfeld, Influence of drying-induced microcracking and related size effects on mass transport properties of concrete, Cement Concr. Res. 68 (2015) 35–48, https://doi.org/10.1016/J.CEMCONRES.2014.10.018.
[48] K. Lyu, W. She, H. Chang, Y. Gu, Effect of fine aggregate size on the overlapping of interfacial transition zone (ITZ) in mortars, Construct. Build. Mater. 248 (2020) 118559, https://doi.org/10.1016/j.conbuildmat.2020.118559.
[49] Q. Song, M.Z. Guo, L. Wang, T.C. Ling, Use of steel slag as sustainable construction materials: a review of accelerated carbonation treatment, Resour. Conserv. Recycl. 173 (2021), https://doi.org/10.1016/j.resconrec.2021.105740.
[50] M.S. Ko, Y.L. Chen, J.H. Jiang, Accelerated carbonation of basic oxygen furnace slag and the effects on its mechanical properties, Construct. Build. Mater. 98 (2015) 286–293, https://doi.org/10.1016/j.conbuildmat.2015.08.051.
[51] M. Tu, H. Zhao, Z. Lei, L. Wang, D. Chen, H. Yu, T. Qi, Aqueous carbonation of steel slag: a kinetics study, ISIJ Int. 55 (2015) 2509–2514, https://doi.org/10.2355/ISIJINTERNATIONAL.ISIJINT-2015-142.
[52] L. Mo, F. Zhang, M. Deng, F. Jin, A. Al-Tabbaa, A. Wang, Accelerated carbonation and performance of concrete made with steel slag as binding materials and aggregates, Cem. Concr. Compos. 83 (2017) 138–145, https://doi.org/10.1016/j.cemconcomp.2017.07.018.
[53] W.C. Wang, Feasibility of stabilizing expanding property of furnace slag by autoclave method, Construct. Build. Mater. 68 (2014) 552–557, https://doi.org/10.1016/J.CONBUILDMAT.2014.06.082.
[54] H.S. Lee, H.S. Lim, M.A. Ismail, Quantitative evaluation of free CaO in electric furnace slag using the ethylene glycol method, Construct. Build. Mater. 131 (2017) 676–681, https://doi.org/10.1016/j.conbuildmat.2016.11.047.
[55] M.P. Javellana, I. Jawed, Extraction of free lime in portland cement and clinker by ethylene glycol, Cement Concr. Res. 12 (1982) 399–403, https://doi.org/10.1016/0008-8846(82)90088-6.
[56] A.S. Brand, J.R. Roesler, Interfacial transition zone of cement composites with steel furnace slag aggregates, Cem. Concr. Compos. 86 (2018) 117–129, https://doi.org/10.1016/J.CEMCONCOMP.2017.11.012.
[57] British Standards Institution BSI, Methods of Testing Cement Part 1, Determination of strength, 2016.
[58] European Committee for Standardizaiton, EN 12457-1, Characterisation of Waste. Leaching, Compliance Test for Leaching of Granular Waste Materials and Sludges, 2014.
[59] Y. Gao, G. De Schutter, G. Ye, H. Huang, Z. Tan, K. Wu, Porosity characterization of ITZ in cementitious composites: concentric expansion and overflow criterion, Construct. Build. Mater. 38 (2013) 1051–1057, https://doi.org/10.1016/j.conbuildmat.2012.09.047.
[60] R. Yang, N.R. Buenfeld, Binary segmentation of aggregate in SEM image analysis of concrete, Cement Concr. Res. 31 (2001) 437–441, https://doi.org/10.1016/S0008-8846(00)00493-2.
[61] S.S. Bangaru, C. Wang, X. Zhou, M. Hassan, Scanning electron microscopy (SEM) image segmentation for microstructure analysis of concrete using U-net convolutional neural network, Autom. ConStruct. 144 (2022) 104602, https://doi.org/10.1016/J.AUTCON.2022.104602.
[62] L. Chen, W. Shan, P. Liu, Identification of concrete aggregates using K-means clustering and level set method, Structures 34 (2021) 2069–2076, https://doi.org/10.1016/J.ISTRUC.2021.08.048.
[63] S. Diamond, J. Huang, The ITZ in concrete – a different view based on image analysis and SEM observations, Cem. Concr. Compos. 23 (2001) 179–188, https://doi.org/10.1016/S0958-9465(00)00065-2.
[64] E. Sánchez, M.T. Deluigi, G. Castellano, Mean atomic number quantitative assessment in backscattered electron imaging, Microsc. Microanal. 18 (2012) 1355–1361, https://doi.org/10.1017/S1431927612013566.
[65] S. Liang, Y. Wei, X. Gao, Z. Qian, Effect of epoxy impregnation on characterizing microstructure and micromechanical properties of concrete by different techniques, J. Mater. Sci. 55 (2020) 2389–2404, https://doi.org/10.1007/S10853-019-04202-3/FIGURES/13.
[66] G.E. Lloyd, Atomic number and crystallographic contrast images with the SEM: a review of backscattered electron techniques, Mineral. Mag. 51 (1987) 3–19, https://doi.org/10.1180/MINMAG.1987.051.359.02.
[67] H.S. Wong, M.K. Head, N.R. Buenfeld, Pore segmentation of cement-based materials from backscattered electron images, Cement Concr. Res. 36 (2006) 1083–1090, https://doi.org/10.1016/J.CEMCONRES.2005.10.006.
[68] R.S. Edwin, M. Mushthofa, E. Gruyaert, N. De Belie, Quantitative analysis on porosity of reactive powder concrete based on automated analysis of back-scattered-electron images, Cem. Concr. Compos. 96 (2019) 1–10, https://doi.org/10.1016/J.CEMCONCOMP.2018.10.019.
[69] N. Otsu, Threshold selection method from gray-level histograms, IEEE Trans Syst Man Cybern. SMC-9 (1979) 62–66, https://doi.org/10.1109/TSMC.1979.4310076.
[70] P.-S. Liao, T.-S. Chen, P.-C. Chung, A fast algorithm for multilevel thresholding, J. Inf. Sci. Eng. 17 (2001) 713–727, https://doi.org/10.6688/JISE.2001.17.5.1.
[71] C. Thomas, J. Rosales, J.A. Polanco, F. Agrela, Steel slags, New Trends Eco-Efficient Recycl. Concr. (2019) 169–190, https://doi.org/10.1016/B978-0-08-102480-5.00007-5.
[72] M. Thommes, K. Kaneko, A.V. Neimark, J.P. Olivier, F. Rodriguez-Reinoso, J. Rouquerol, K.S.W. Sing, Physisorption of gases, with special reference to the evaluation of surface area and pore size distribution (IUPAC Technical Report), Pure Appl. Chem. 87 (2015) 1051–1069, https://doi.org/10.1515/pac-2014-1117.
[73] S. Brunauer, P.H. Emmett, E. Teller, Adsorption of gases in multimolecular layers, J. Am. Chem. Soc. 60 (1938) 309–319, https://doi.org/10.1021/JA01269A023/ASSET/JA01269A023.FP.PNG_V03.
[74] E.P. Barrett, L.G. Joyner, P.P. Halenda, The determination of pore volume and area distributions in porous substances. I. Computations from nitrogen isotherms, J. Am. Chem. Soc. 73 (1951) 373–380, https://doi.org/10.1021/JA01145A126/ASSET/JA01145A126.FP.PNG_V03.
[75] K. Scrivener, R. Snellings, B. Lothenbach, A practical guide to microstructural analysis of cementitious materials, A Pract. Guid. to Microstruct. Anal. Cem. Mater. (2016) 1–531, https://doi.org/10.1201/B19074.
[76] H. Ma, Z. Li, Realistic pore structure of Portland cement paste: experimental study and numerical simulation, Comput. Concr. 11 (2013) 317–336, https://doi.org/10.12989/cac.2013.11.4.317.
[77] K.K. Aligizaki, Pore Structure of Cement-Based Materials, CRC Press, 2005, https://doi.org/10.1201/9781482271959.
[78] R. Ševčík, P. Šašek, A. Viani, Physical and nanomechanical properties of the synthetic anhydrous crystalline CaCO3 polymorphs: vaterite, aragonite and calcite, J. Mater. Sci. 53 (2018) 4022–4033, https://doi.org/10.1007/S10853-017-1884-X/TABLES/3.
[79] Ç.M. Oral, B. Ercan, Influence of pH on morphology, size and polymorph of room temperature synthesized calcium carbonate particles, Powder Technol. 339 (2018) 781–788, https://doi.org/10.1016/J.POWTEC.2018.08.066.
[80] O. Cherkas, T. Beuvier, F. Zontone, Y. Chushkin, L. Demoulin, A. Rousseau, A. Gibaud, On the kinetics of phase transformations of dried porous vaterite particles immersed in deionized and tap water, Adv. Powder Technol. 29 (2018) 2872–2880, https://doi.org/10.1016/J.APT.2018.08.008.
[81] T.S. Naidu, C.M. Sheridan, L.D. van Dyk, Basic oxygen furnace slag: review of current and potential uses, Miner. Eng. 149 (2020), https://doi.org/10.1016/j.mineng.2020.106234.
[82] P. Chaurand, J. Rose, O. Proux, J.L. Hazemann, V. Briois, M. Salome, J. Susini, J. H. Ferrasse, D. Borschneck, J.Y. Bottero, Environmental impact of steel slag reused as aggregates in road manufacturing: molecular mechanisms of chromium and vanadium release, AIP Conf. Proc. 882 (2007) 199–201, https://doi.org/10.1063/1.2644473.
[83] P. Chaurand, J. Rose, J. Domas, J.Y. Bottero, Speciation of Cr and V within BOF steel slag reused in road constructions, J. Geochem. Explor. 88 (2006) 10–14, https://doi.org/10.1016/j.gexplo.2005.08.006.
[84] A.M. Kaja, S. Melzer, H.J.H. Brouwers, Q. Yu, On the optimization of BOF slag hydration kinetics, Cem. Concr. Compos. 124 (2021) 104262, https://doi.org/10.1016/J.CEMCONCOMP.2021.104262.
[85] A. van Zomeren, S.R. van der Laan, H.B.A. Kobesen, W.J.J. Huijgen, R.N. J. Comans, Changes in mineralogical and leaching properties of converter steel slag resulting from accelerated carbonation at low CO 2 pressure, Waste Manag. 31 (2011) 2236–2244, https://doi.org/10.1016/j.wasman.2011.05.022.
[86] Soil Quality Decree, 2015. https://wetten.overheid.nl/BWBR0023085/2015-07-01#BijlageA.
[87] W. Schwarz, Novel cement matrices by accelerated hydration of the ferrite phase in portland cement via chemical activation: kinetics and cementitious properties, Adv. Cement Base Mater. 2 (1995) 189–200, https://doi.org/10.1016/1065-7355(95)90003-9.
[88] S. Smillie, F.P. Glasser, Reaction of EDTA, oxalic acid and citric acid with Portland cement, Adv. Cement Res. 11 (1999) 97–101, https://doi.org/10.1680/adcr.1999.11.2.97.
[89] A.J. Francis, C.J. Dodge, J.B. Gillow, Biodegradation of metal citrate complexes and implications for toxic-metal mobility, Nat 1992 3566365. 356 (1992) 140–142, https://doi.org/10.1038/356140a0.
[90] S. Diamond, Considerations in image analysis as applied to investigations of the ITZ in concrete, Cem. Concr. Compos. 23 (2001) 171–178, https://doi.org/10.1016/S0958-9465(00)00085-8.
[91] M.H.N. Yio, M.J. Mac, H.S. Wong, N.R. Buenfeld, 3D imaging of cement-based materials at submicron resolution by combining laser scanning confocal microscopy with serial sectioning, J. Microsc. 258 (2015) 151–169, https://doi.org/10.1111/JMI.12228.

[92] T. Akçaoğlu, M. Tokyay, T. Çelik, Assessing the ITZ microcracking via scanning electron microscope and its effect on the failure behavior of concrete, Cement Concr. Res. 35 (2005) 358–363, https://doi.org/10.1016/j.cemconres.2004.05.042.

[93] H.S. Wong, M. Zobel, N.R. Buenfeld, R.W. Zimmerman, Influence of the interfacial transition zone and microcracking on the diffusivity, permeability and sorptivity of cement-based materials after drying, Mag. Concr. Res. 61 (2009) 571–589, https://doi.org/10.1680/MACR.2008.61.8.571/ASSET/IMAGES/SMALL/MACR61-571-F7.GIF.

[94] Y. Zhou, J. Sun, Y. Liao, Influence of ground granulated blast furnace slag on the early hydration and microstructure of alkali-activated converter steel slag binder, J. Therm. Anal. Calorim. (2020) 1–10, https://doi.org/10.1007/S10973-020-10220-0/FIGURES/10.

[95] Y. Ma, G. Ye, The shrinkage of alkali activated fly ash, Cement Concr. Res. 68 (2015) 75–82, https://doi.org/10.1016/J.CEMCONRES.2014.10.024.